P wave tomography for 3-D radial and azimuthal anisotropy beneath Greenland and surrounding regions

Genti Toyokuni[1*] and Dapeng Zhao[1]

[1] Department of Geophysics, Graduate School of Science, Tohoku University, Sendai 980-8578, Japan

Submitted to ***Tectonics*** in March 2021

*Corresponding author:

Genti Toyokuni

E-mail: toyokuni@tohoku.ac.jp

ORCID ID: 0000-0003-3786-207X

Key Points:

- 3-D *P*-wave radial and azimuthal anisotropy structure of the upper mantle beneath Greenland and surrounding regions is investigated.
- The presence of upper-mantle plumes beneath Iceland, Jan Mayen, and Svalbard hotspots is confirmed from seismic anisotropy.
- A new scenario for the breakup between Greenland and Canada is proposed.

Abstract

We present the first 3-D images of *P*-wave radial anisotropy (RAN) and azimuthal anisotropy (AAN) down to 750-km depth beneath Greenland and surrounding regions. The results are obtained by applying a regional tomographic method to simultaneously invert *P* wave arrival times of 1,309 local events and *P* wave relative traveltime residuals of 7,202 teleseismic events, which were recorded mainly by the latest GLISN network. A high-velocity body located beneath northeast Greenland (NEG) to its offshore exhibits a strong negative RAN and a strong AAN with N-S to NE-SW oriented fast-velocity directions (FVDs). The FVDs are generally consistent with the direction of the fold axis of the Caledonian fold belt, which is considered as an outcrop of the NEG body on land. Beneath the Iceland, Jan Mayen, and Svalbard hotspots, a strong positive RAN and a negligible or weak AAN are revealed, which may reflect effects of upwelling mantle plumes. Among the three regions, a weak AAN with a constant FVD is only revealed beneath Iceland, which may reflect the existence of background mantle flow. The RAN and AAN features beneath the Labrador Sea, Davis Strait, and Baffin Bay suggest the following scenario on breakup between Greenland and Canada: the breakup was initiated at the Labrador Sea due to local mantle upwelling, but the northward propagation of the breakup was blocked by a strong high-velocity anomaly beneath Davis Strait; the opening of Baffin Bay might be caused passively by far-field plate forces.

1. Introduction

Greenland is the largest island in the world whose land area spans over 20° in the central angle of the Earth. The surface-exposed rocks have preserved ~4 billion years of Earth's history in the oldest part (Henriksen et al., 2009). However, the Greenland Ice Sheet (GrIS), covering 80% of the land area, has long been preventing the geological study in the inland area. Greenland

itself has low seismic activity and no known active volcanoes, but there are several hot springs on the east and west coasts of Greenland (Hjartarson & Armannsson, 2010) that coincide with Tertiary basalt outcrops. The Mid-Atlantic Ridge (MAR) is located on the eastern side of Greenland, where the North American plate and the Eurasian plate separate from each other, inducing very active seismicity. There are also three major hotspots (Iceland, Jan Mayen, and Svalbard) along the MAR, highlighting the tectonic activity of this region. Turing our eyes to the western side of Greenland, Baffin Bay, Davis Strait, and Labrador Sea separate Greenland and Canada (Figure 1).

Currently, 34 seismic stations, including four on the GrIS, are in operation in and around Greenland by the Greenland Ice Sheet monitoring Network (GLISN) launched in 2009 (Clinton et al., 2014; Toyokuni et al., 2014). Seismological studies using the GLISN data have been made actively (e.g., Darbyshire et al., 2018; Lebedev et al., 2017; Levshin et al., 2017; Mordret, 2018; Mordret et al., 2016; Pourpoint et al., 2018; Rickers et al., 2013; Toyokuni et al., 2015, 2018, 2020a, 2020b, 2021), but only a few of them focused on the mantle structure using body wave data (Rickers et al., 2013; Toyokuni et al., 2020a, 2020b).

Toyokuni et al. (2020a) conducted, for the first time, the detailed body wave (*P* wave) tomography in and around Greenland to investigate the 3-D *P*-wave velocity (V_P) structure down to 700-km depth. Their results are summarized as follows. (1) In the upper mantle beneath the Iceland, Jan Mayen and Svalbard hotspots, there are Iceland plume, Jan Mayen plume, and Svalbard plume, respectively, which extend almost vertically down to the mantle transition zone (MTZ) where the three plumes merge together. (2) A low-V_P anomaly, elongating in the NW-SE direction, was revealed at depths $\leq$ 250 km beneath central Greenland, forming the central Greenland lithospheric low-velocity zone (CGLLVZ). The CGLLVZ is interpreted as a

polymerization of ancient Iceland and Jan Mayen plume tracks due to plate movement. (3) A high-V_P body was revealed at depths ≤ 500 km off the northeastern coast of Greenland. This body seems continuous to the Caledonian fold belt in northeast Greenland, and so was interpreted as a remnant of oceanic lithosphere constituted the Iapetus Ocean, closed 490−390 Ma, due to collision of Laurentia and Baltica (Henriksen et al., 2009; Metelkin et al., 2015). This body is located inside the bend of MAR that is thought to have existed at the time of the North Atlantic opening (Thiede et al., 2011); therefore, this body may have restricted the mode of plate expansion. Furthermore, this body seems to act as an obstacle separating flows of the Jan Mayen and Svalbard plumes. Hereinafter, we call it the "Northeast Greenland (NEG) body."

Now that the static structural features described above have been revealed, we are interested in dynamic features of the region. Seismic anisotropy shows a direction-dependent nature of the Earth's material on seismic wave propagation, which is widely revealed from the crust and mantle to the inner core (Long & Becker, 2010). Seismic anisotropy in the mantle is generally induced by the lattice-preferred orientation (LPO) of olivine. There are several olivine types (A-, B-, C-, D-, and E-types) in the upper mantle, which exhibit different relationships between the anisotropic structure and the dominant slip system. However, these olivine fabrics except for B-type exhibit a fast axis parallel to the mantle flow direction (Karato et al., 2008). The B-type olivine only appears in an environment of high-stress, low-temperature, and water-rich conditions (Katayama & Karato, 2006).

So far, only a few studies have investigated seismic anisotropy in Greenland, Iceland, and surrounding regions, using surface wave tomography (Darbyshire et al., 2018), shear-wave splitting (SWS) measurements (Bjarnason et al., 2002; Ucisik et al., 2005, 2008), and numerical modeling of mantle flow (Marquart et al., 2007). Darbyshire et al. (2018) conducted surface

89 wave tomography to investigate azimuthal anisotropy of Rayleigh-wave group velocity in the
90 crust and uppermost mantle beneath Greenland. However, the depth they analyzed was limited to
91 <~100 km due to the frequency band of the Rayleigh wave. Measuring SWS is a popular method
92 to obtain the azimuthal fast-polarization orientation (FPO) and time delay of the medium directly
93 beneath a station using, for example, *SKS* and *SKKS* phases that have rays close to the vertical
94 direction. The depth range of the medium that provides FPO can be estimated from the degree of
95 time delay, but the depth resolution is not good. To date, there has been no study of the 3-D
96 anisotropic structure beneath Greenland and its surrounding regions using body waves that
97 penetrate deeply into the mantle and so have a good depth resolution.

98 Seismic anisotropy tomography using body waves is the updated method to constrain 3-D
99 images of both radial anisotropy (RAN) and azimuthal anisotropy (AAN) of the subsurface
100 structure (e.g., Ishise & Oda, 2005; Wang & Zhao, 2008, 2013; Zhao, 2015). This method has
101 been applied to various regions in the world, for example, Japan (Ishise & Oda, 2005; Liu &
102 Zhao, 2017; Wang & Zhao, 2021), Alaska (Gou et al., 2019), and Southeast Asia (Huang et al.,
103 2015). However, it has been rarely applied to areas where a mid-ocean ridge or a mantle plume
104 exists, except for the Erebus hotspot in Antarctica (Zhang et al., 2020). The purpose of this study
105 is to determine the first 3-D *P*-wave RAN and AAN model of the upper mantle beneath the study
106 region (Figure 2a) by analyzing the GLISN data to improve our understanding of the subsurface
107 structure and mantle dynamics of this region.

108 **2. Method**

109 We apply a regional tomography method to *P*-wave travel-times from both local and
110 teleseismic events (Zhao et al., 1994, 2012; Toyokuni et al., 2020a). For the local events, we use
111 travel-time residuals (t_{ij}):

$$t_{ij} = T_{ij}^{\mathrm{OBS}} - T_{ij}^{\mathrm{CAL}} \tag{1}$$

where T_{ij}^{OBS} and T_{ij}^{CAL} are observed and calculated (theoretical) arrival times, respectively, from the ith event to the jth station. For the teleseismic events, we use relative travel-time residuals (r_{ij}):

$$\begin{aligned} r_{ij} &= t_{ij} - \overline{t_i} \\ \overline{t_i} &= \frac{1}{n_i}\sum_{j=1}^{n_i} t_{ij} \end{aligned} \tag{2}$$

where n_i is the number of recording stations of the ith event, and $\overline{t_i}$ is the average of travel-time residuals at the n_i stations. Note that $\overline{t_i}$ includes the influence of structural heterogeneity outside the study volume as well as errors in the hypocentral parameters. In the tomographic inversion, we only consider the teleseismic ray segments that are located within the study volume.

We conduct tomographic inversions for 3-D *P*-wave RAN and AAN using the method of Wang & Zhao (2008, 2013). In a RAN medium, the symmetry axis is assumed to be in the vertical direction, and one parameter is added to express anisotropy. The total slowness (S) due to RAN can be written as

$$S = \frac{1}{V_{P0}}(1 + M\cos 2i) \tag{3}$$

where V_{P0} is isotropic *P*-wave velocity, M is the strength of anisotropy, and i is the ray path incident angle (Wang & Zhao, 2008). The amplitude of RAN α can be represented as

$$\alpha = \frac{V_{Ph} - V_{Pv}}{2V_{P0}} = \frac{M}{1 - M^2} \tag{4}$$

where V_{Ph} and V_{Pv} are *P*-wave velocities in the horizontal and vertical directions, respectively. Therefore, positive values of α represent that the horizontally propagating *P*-wave travels faster than the vertically propagating one ($V_{P\mathrm{h}} > V_{Pv}$), and vice versa.

In an AAN medium, the symmetry axis is assumed to be in a horizontal plane, and two parameters are adopted to express AAN. The total slowness (S) due to AAN can be written as

$$S = \frac{1}{V_{P0}}[1 + A\cos 2\phi + B\sin 2\phi] \tag{5}$$

where A and B are two azimuthal anisotropy parameters, and ϕ is the ray path azimuth (Wang & Zhao, 2013). The amplitude of AAN β and fast velocity direction (FVD) ψ can be expressed as

$$\beta = \frac{V_{Pf} - V_{Ps}}{2V_{P0}} = \frac{\sqrt{A^2 + B^2}}{1 - (A^2 + B^2)^2} \tag{6}$$

$$\psi = \begin{cases} \frac{1}{2}\tan^{-1}\left(\frac{B}{A}\right) + \begin{cases} \frac{\pi}{2} & (A > 0) \\ 0 & (A < 0) \end{cases} \\ -\frac{\pi}{4} \quad (A = 0, B > 0) \\ \frac{\pi}{4} \quad (A = 0, B < 0) \end{cases} \tag{7}$$

where V_{Pf} and V_{Ps} are *P*-wave velocities in the fast and slow directions, respectively.

We first determine a 3-D isotropic V_P model using the seismic tomography method of Zhao et al. (1994, 2012), which discretizes the study volume using a 3-D grid. We conduct global coordinate transformation of the study region by moving its center to the equator (Takenaka et al., 2017; Toyokuni et al., 2020a), so that we can set 3-D grid nodes for the tomographic inversion uniformly both in the latitude and longitude directions. Following Toyokuni et al. (2020a), we move the station SUMG (longitude, latitude)=(−38.461°, 72.574°) on the GrIS summit to a point on the equator $(90°, 0°)$. We then arrange 2-D grid meshes in the area between 70° and 120° longitude and −20° and 20° latitude, after the coordinate transformation (Figure 2a). For the isotropic 3-D V_P structure (V_{P0}), we adopt a horizontal grid interval of 2° in both latitude and longitude directions, and the 2-D grid meshes are set at depths of 5, 20, 40, 60, 80, 100, 120, 140, 160, 190, 220, 250, 280, 310, 340, 370, 400, 430, 460, 490, 520, 550, 580, 610, 640, 670, 700, 750, 800, 850, and 900 km (Figure S1a). For the V_P anisotropic components (M for the RAN, or A and B for the AAN), we adopt a horizontal grid interval of 3° in both latitude and longitude directions, and 2-D grid meshes are set at depths of 5, 20, 60, 100, 140, 190, 250, 310, 370, 430, 490, 550, 610, 670, and 750 km (Figure S1b). Note that, to solve the anisotropic components at the grid nodes, we need seismic rays from various directions with a sufficient density. Hence, we set the grid nodes for the anisotropy coarser than those for solving the isotropic component. Tomographic inversions for the 3-D RAN and AAN structures are conducted separately because of the different assumptions on the symmetry axis for RAN and AAN.

Theoretical travel times are calculated by using a 3-D ray tracing technique that combines the pseudo-bending scheme (Um & Thurber, 1987) and Snell's law (Zhao et al., 1992). The initial 1-D model for the isotropic component is shown in Figure S2. The initial values of the

anisotropic parameters are set to zero. The Conrad and Moho depths are fixed at 20 and 40 km, respectively. We conduct the tomographic inversions using the LSQR algorithm (Paige & Saunders, 1982) with damping and smoothing regularizations (Zhao et al., 1992, 1994, 2012; Wang & Zhao, 2008, 2013).

3. Data

The data used in this study are the updated version of those used in Toyokuni et al. (2020a). We first downloaded all *P*-wave arrival time data of $M \geq 3$ earthquakes observed at 33 GLISN stations and one temporary station (station code: IC-GL) on the GrIS during January 1964 to December 2016 from the ISC-EHB catalog (http://www.isc.ac.uk/isc-ehb/). To extract local earthquake data, the coordinate transformation (Section 2) is first applied to all the epicenters and station locations. Earthquakes that occurred between 70° and 120° longitude, and −20° and 20° latitude were then extracted as local earthquakes. All earthquakes recorded at one or more stations were extracted. As a result, 2,414 *P*-wave arrival times from 1,288 local events were obtained (Figure 2a). The magnitudes of these extracted events range from 3.1 to 7.1, with focal depths between 0.0 and 31.5 km. To extract teleseismic events, earthquakes with epicentral distances between 30° and 100° and recorded at five or more stations in the study region were extracted. As a result, 51,578 *P*-wave arrival times from 7,088 teleseismic events were obtained.

We then manually picked 781 *P*-wave and 541 *S*-wave arrival times from 43 local events recorded at 34 GLISN stations from waveforms downloaded from the IRIS/DMC (https://ds.iris.edu/ds/nodes/dmc/) (Figures S3 and S4). We relocated the 43 events using both *P*- and *S*-wave arrival times, and extracted those events with five or more data with absolute travel-time residuals within ±3 s for both *P*- and *S*-wave data, and with uncertainty of the focal depth ≤

20 km. After this processing, 407 *P*-wave arrival times from 21 local events remain in the data set (Figure 2a). The *S*-wave data are not used in the subsequent analysis.

We also added teleseismic *P*-wave relative arrival-time data picked by Toyokuni et al. (2020a), which contain 7,573 picks from 347 teleseismic events that occurred from January 1, 2012 to July 15, 2019. When the event overlaps with those in the ISC catalog, the ISC data are removed. As a result, we obtained 56,498 *P*-wave arrival times (51,578 − 2,653 + 7,573) from 7,231 teleseismic events (7,088 – 204 + 347). We then applied crustal correction to the teleseismic data according to the method of Jiang et al. (2009a, 2009b, 2015) and Toyokuni et al. (2020a). Figures S5a and S5b show the distributions of the relative travel-time residuals averaged at each station for all events, both before and after the crustal correction. During the process, any teleseismic data with relative travel-time residuals exceeding ±3 s are further discarded. As a result, the number of teleseismic events and the number of relative travel-time residuals are 7,202 and 55,917, respectively, before the crustal correction, and 7,202 and 55,768, respectively, after the correction (Figure 2b). The final dataset used for our tomographic inversions includes these teleseismic data and 2,821 *P*-wave arrival times (2,414 + 407) from 1,309 local earthquakes (1,288 + 21) obtained from the ISC-EHB catalog and our manual picking. Figure S6 shows the distribution of the local and teleseismic rays used in this study.

4. Results

4.1 Isotropic tomography

We first conduct a tomographic inversion for the 3-D isotropic V_P structure with exactly the same grid and parameter settings as Toyokuni et al. (2020a) using our new data set. Map views and vertical cross-sections of the results are shown in Figure S7, and Figures S8−S9,

213 respectively. All the features described in Section 1 are well visible in these results, confirming
214 the robustness of the images obtained by the isotropic V_P tomography.

215 **4.2 Radial anisotropy (RAN)**

216 Figure 3 shows map views of the obtained RAN tomography. Focusing on the isotropic
217 component, the NEG body is clearly imaged as the most prominent high-velocity (high-V_{P0})
218 region at depths ≤ 490 km beneath the northeastern coast of Greenland to the northeastern
219 offshore. High-V_{P0} anomalies are also visible from northwestern Greenland to Ellesmere Island
220 at depths ≤ 490 km, and beneath the southern tip of Greenland at depths ≥ 430 km. The most
221 prominent low-velocity (low-V_{P0}) anomalies are related to hotspots beneath Iceland, Jan Mayen,
222 and Svalbard from the surface down to 610 km depth. At depths ≤ 250 km, a low-V_{P0} anomaly is
223 also visible beneath inland Greenland elongated in the NW-SE direction and extend to the
224 Iceland and Jan Mayen hotspots (the CGLLVZ). These isotropic V_P features are in very good
225 agreement with the previous results of isotropic tomography (Toyokuni et al., 2020a and Section
226 4.1), although the anisotropic tomography is obtained by stronger smoothing, and so the features
227 are much blunt.

228 Regarding the anisotropic features, reliable results are obtained at depths of 190−550 km
229 according to the resolution tests shown in the followings. The most prominent negative RAN
230 ($\alpha < 0$, i.e., $V_{P\mathrm{h}} < V_{Pv}$, as shown in vertical bars in Figure 3) can be seen beneath the NEG body.
231 Weak negative RAN is also found along the coast of western Greenland at depths ≤ 310 km, but
232 nothing else is prominent. In contrast, positive RAN ($\alpha > 0$, i.e., $V_{P\mathrm{h}} > V_{Pv}$, as shown in
233 horizontal bars in Figure 3) can be found at all depths and in various parts of the study region.
234 The most notable ones are located in the low-V zones just beneath the Iceland, Jan Mayen, and
235 Svalbard hotspots. There is another remarkable positive RAN beneath Davis Strait and the

Labrador Sea at depths ≤ 490 km, but no significant anisotropy is found beneath Baffin Bay. No significant anisotropy is observed in the low-V_{P0} zone running in the NW-SE direction beneath central Greenland at depths ≤ 250 km, and in the high-V_{P0} zone beneath the southern tip of Greenland at depths ≥ 430 km.

Vertical cross-sections are shown in Figures 4 and 5. In the cross-sections through Iceland, Jan Mayen, and Svalbard (e.g., J-J' and K-K' sections in Figure 4a), a low-V_{P0} anomaly extending from the mantle transition zone (MTZ) and a strong positive RAN ($V_{P\mathrm{h}} > V_{Pv}$) are remarkable. A strong negative RAN ($V_{P\mathrm{h}} < V_{Pv}$) in the high-V_{P0} body in the upper mantle between Jan Mayen and Svalbard is also characteristic. In the cross-sections from Iceland to central Greenland (e.g., C-C' sections in Figure 5a), the low-V_{P0} zone suddenly thins to a depth ≤ 250 km when entering the Greenland side beyond Denmark Strait, and a positive RAN ($V_{P\mathrm{h}} > V_{Pv}$) weakens in the thinned low-V_{P0} zone. The upper mantle beneath the Labrador Sea is characterized by a weak low-V_{P0} anomaly and a moderate positive RAN ($V_{P\mathrm{h}} > V_{Pv}$). Overall, the characteristics of the isotropic component are in good agreement with the results of isotropic tomography. However, in the anisotropic tomography, the grid is coarse and the smoothing is set to be strong, so the resolution becomes lower. For example, the Iceland plume and the Jan Mayen plume are not separated, and the CGLLVZ looks thicker than that in the isotropic tomography.

4.3 Azimuthal anisotropy (AAN)

Figure 6 shows map views of the obtained AAN tomography. Regarding the anisotropic features, reliable results are obtained at depths of 190−550 km according to the resolution tests shown in the followings. The regions with marked AAN at depths ≤ 430 km are the interior of the NEG body and the region beneath Davis Strait to southwestern Greenland. The NEG body

corresponds well to the strong AAN that exhibits N-S to NW-SE FVDs. On the other hand, the AAN in southwestern Greenland does not clearly correspond to the high-V_{P0} anomaly, and the predominant FVDs are NE-SW to E-W. No significant AAN is seen in central Greenland, which appears to separate these two regions. Even at depths of 490 and 550 km, the overall characteristics do not change largely. The NEG body is obscured, but the AAN still remains, exhibiting N-S to NE-SW FVDs. The predominant FVD in southwestern Greenland is E-W. No strong AAN appears beneath the Iceland, Jan Mayen, and Svalbard hotspots. However, only beneath Iceland, a weak AAN with N-S to NW-SE FVDs occurs at depths of 190−550 km.

Vertical cross-sections are shown in Figures 7 and 8. The characteristics of the isotropic component are almost the same as those of RAN tomography. In the cross-sections through Iceland, Jan Mayen, and Svalbard (e.g., J-J' and K-K' sections in Figure 7a), a weak AAN with NNW-SSE FVDs appears at depths ≤ 600 km beneath Iceland, but the AAN is hardly seen beneath Jan Mayen and Svalbard. The high-V_{P0} body in the upper mantle between Jan Mayen and Svalbard has a remarkable AAN with N-S to NE-SW FVDs. In the cross-sections from Iceland to central Greenland (e.g., C-C' sections in Figure 8a), the AAN weakens in the thinned low-V_{P0} zone beneath central Greenland. In the cross-sections through Baffin Island and western Greenland, a moderate AAN with NE-SW FVD is predominant in the upper mantle beneath Davis Strait, which continues to a region beneath the west coast of Greenland. The similar AAN seems to extend to a region beneath Baffin Island, but here N-S FVDs are more predominant. Going further south and looking at the cross-sections through the Labrador Sea, the AAN weakens in and around the low-V_{P0} zone at depths ≤ 300 km, but a stronger AAN with E-W FVDs becomes prominent at depths of 300−500 km.

After making many tomographic inversions, the number of iterations is set to three for both the RAN and AAN tomography, and the damping parameters in the 1st, 2nd, and 3rd iterations are set to 20, 50, and 100, respectively. The smoothing parameter is set to 20,000 for both the isotropic and anisotropic components in the RAN and AAN tomography. For comparison, we conducted another inversion for only the isotropic component with the same parameters and grid settings (Figures S10−S12). The final root-mean-square (RMS) travel-time residual is 0.648 s after the inversion for only the isotropic component, 0.616 s for RAN, and 0.607 s for AAN, indicating that the 3-D velocity model fits the data better when anisotropy is included in the inversion (Figure 9).

5. Resolution tests

We conducted many resolution tests, including restoring resolution tests (RRTs) (Zhao et al., 1992), trade-off tests (TOTs), and synthetic resolution tests (SRTs), to evaluate the ray coverage and spatial resolution of our models.

For the RAN tomography, three tests (RAN-RRT, RAN-TOT1, and RAN-TOT2, see Table 1) are conducted. The RAN-RRT is the RRT that highlights the patterns in the main RAN tomographic results when constructing the input model. To create the input model for the isotropic component, at grid nodes with V_{P0} anomalies > +0.6% or < −0.6% in the RAN tomographic results, constant V_{P0} anomalies of +3% or −3% are assigned. For the anisotropic component, at grid nodes with α > +1.0% or < −1.0% in the RAN tomographic results, constant α of +2% or −2% are assigned. The isotropic V_P perturbation and anisotropy at the other grid nodes are set to zero. The RAN-TOT1 is a TOT to examine the trade-off between isotropic V_P and anisotropy, and its input model contains only the isotropic component. The RAN-TOT2 is

another TOT to examine the trade-off, but its input model contains only the anisotropic component.

For the AAN tomography, five tests (AAN-RRT, AAN-TOT1, AAN-TOT2, AAN-SRT1, and AAN-SRT2, see Table 1) are conducted. The AAN-RRT is a RRT that highlights the patterns in the main AAN tomographic results when constructing the input model. To create the input model for the isotropic component, at grid nodes with V_{P0} anomalies > +0.6% or < −0.6% in the main AAN tomographic results, we assign constant V_{P0} anomalies of +3% or −3%. For the anisotropic component, at grid nodes with β > +1.0% or < −1.0% in the AAN tomographic results, we assign constant β of +2% or −2%. As for the FVD, at the grid nodes where FVD is in the range from −45.0° to −22.5°, from −22.5° to 22.5°, from 22.5° to 67.5°, from 67.5° to 112.5°, and from 112.5° to 135.0° in the main AAN tomographic results, we assign a constant value of −45.0°, 0.0°, 45.0°, 90.0°, and −45.0°, respectively, in the RRT input model. The isotropic V_P perturbation and anisotropy at the other grid nodes are set to zero. As in the case of RAN tomography, AAN-TOT1 and AAN-TOT2 are performed to examine the trade-off from isotropic V_P to anisotropy and from anisotropy to isotropic V_P, respectively. The AAN-SRT1 and AAN-SRT2 are two SRTs whose input model contains synthetic anisotropic anomalies, whereas its isotropic component is the same as that in the AAN-RRT input model.

Synthetic data sets for all the RRT, TOT, and SRT inversions for both the RAN and AAN cases are constructed by calculating theoretical arrival times for each input model but with random errors added, which range between −0.3 and +0.3 s with a standard deviation of 0.1 s. Main features of the test results are summarized in Figures 10 and 11 for the RAN and AAN cases, respectively. Details of the test results are shown in supporting information for the RAN-

RRT (Figure S13), RAN-TOT1 (Figure S14), RAN-TOT2 (Figure S15), AAN-RRT (Figure S16), AAN-TOT1 (Figure S17), AAN-TOT2 (Figure S18), AAN-SRT1 (Figure S19), and AAN-SRT2 (Figure S20).

Regarding the RAN-RRT results (Figures 10a and S13), due to strong smoothing in the inversion of this study, both isotropic and anisotropic components spread more widely than those in the input model. However, main features of both the isotropic and anisotropic components are generally recovered at depths of 100−750 km, although the recovery of anisotropic component is slightly worse at depths of 670 and 750 km. Regarding the RAN-TOT1 results (Figures 10b and S14), the isotropic component is well recovered at all depths. On the other hand, exudation from the isotropic to anisotropic component can be confirmed at depths of 190−490 km. However, the pattern of anisotropy is different from that of the main RAN tomographic results (Figure 3), and the maximal intensity of anisotropy is about 60% of those for the RAN-RRT case, so the influence of trade-off on the tomographic result is considered to be small. Regarding the RAN-TOT2 results (Figures 10c and S15), the anisotropy pattern is well recovered at depths ≤ 670 km, and there is almost no leakage from the anisotropy to isotropic V_P.

Similar to the RAN case, the effect of smoothing can be seen in the AAN-RRT results (Figures 11a and S16), but the characteristics of both isotropic and anisotropic components can be recovered well at depths of 100−750 km. The AAN-TOT1 results (Figures 11b and S17) show that the isotropic components are well recovered at all depths. The leakage from the isotropic to anisotropic components becomes remarkable at depths ≥ 610, but the intensity is weak at other depths, and the pattern is also significantly different from that of the main AAN tomographic results. Regarding the AAN-TOT2 results (Figures 11c and S18), the anisotropic characteristics are well recovered at depths ≤ 610 km, and there is almost no leakage from the

anisotropic to isotropic components. The AAN-SRT1 (Figures 11d and S19) and AAN-SRT2 (Figures 11e and S20) results show that the pattern of isotropic component is slightly distorted by the strong artificial anisotropic components. However, the intensity of anisotropy and FVDs are well recovered in both cases at depths of 100−550 km. In particular, the input FVDs in the AAN-SRT1 case are well recovered, although these have a sense that is orthogonal to the anisotropic pattern obtained by the main AAN tomographic results, confirming the reliability of the FVDs obtained by the main AAN tomography.

6. Discussion

According to the resolution tests in Section 5, we here discuss the structure at depths of 190−550 km. The RAN and AAN tomographic results in this depth range do not change largely at any depth, whose characteristics are represented by the map views at a depth of 310 km that are enlarged in Figures 12a and 12b. Figure 12c summarizes the characteristics of isotropic component, RAN, and AAN for seven areas (NEG body, Iceland hotspot, Jan Mayen hotspot, Svalbard hotspot, Labrador Sea, Davis Strait, and Baffin Bay). First, the characteristics of AAN (Figure 12b) beneath Greenland are compared with the SWS measurements (Figure 12d) by Ucisik et al. (2008). The SWS feature is estimated to be mainly in the upper mantle, but some contributions from the crust and lower mantle maybe present (Ucisik et al., 2008). The overall characteristics of the two results are similar: for example, FVD along coastline is dominant beneath the northeastern coast of Greenland, no apparent anisotropy can be observed beneath the SUMG station in central Greenland, and FVD in the NE-SW direction is dominant beneath the west coast of Greenland. Different from the SWS measurements that have poor depth resolution, the anisotropic tomography reveals 3-D isotropic and anisotropic structures, which brings more

detailed insights into the static and dynamic features. In the following, we discuss main features in each of the seven areas in Figures 12a−12c.

6.1 The Northeast Greenland body.

The NEG body is characterized by a high-V_{P0} anomaly, a strong negative RAN ($V_{Ph} < V_{Pv}$), and a strong AAN with N-S to NE-SW FVDs. This body is presumed as a remnant of the oceanic lithosphere that made up the Iapetus Ocean closed at 490−390 Ma. The causes of seismic anisotropy in such a cold rock body may be (1) fossil anisotropy originally possessed by the oceanic lithosphere, (2) shape-preferred orientation (SPO) associated with the shape and texture of the rock body, and (3) LPO accompanying with mantle flow. Since both the isotropic and anisotropic characteristics inside the NEG body are clearly different from those in the surrounding regions, we consider that (1) and (2) are primarily responsible. In particular, regarding (2), since the NEG body includes the inland Caledonian fold belt, which has a fold axis in the N-S direction, we expect that the FVDs are likely to be dominant along the fold axis (Okaya et al., 2018), and that the weight of the rock body causes consolidation resulting in $V_{Ph} < V_{Pv}$. Such an interpretation well explains the results of this study.

6.2 Iceland, Jan Mayen, and Svalbard hotspots

The upper mantle beneath the Iceland hotspot is characterized by a strong positive RAN ($V_{Ph} > V_{Pv}$) and a weak AAN with NW-SE FVDs, which may primarily be associated with the Iceland plume. The Iceland plume is one of the strongest buoyant plumes in the world, and so is estimated that the rising rate of mantle material in the center of the plume is extremely fast. Possible causes of anisotropy in such plumes are (1) LPO associated with the flow of the plume and the surrounding mantle, and (2) SPO due to the shape of the plume and the heterogeneous

392 distribution of mantle materials with different temperatures. Regarding (1), the vertical LPO is
393 dominant in the plume center, whereas in the surrounding regions, the mantle flow is drawn
394 toward or diverges from the plume center, creating a radial flow field that dominates horizontal
395 LPO (Marquart et al., 2007). Regarding (2), low-V material continues in the vertical direction
396 along the rising plume, whereas in the horizontal direction, the material properties change from
397 low-V at the plume center to high-V in the surrounding regions, resulting in horizontal FVDs that
398 are distributed radially from the plume center. Therefore, in both cases, the feature of $V_{P\mathrm{h}} > V_{Pv}$
399 appears macroscopically, and a weak or negligible AAN is expected by canceling out the radial
400 FVDs. Such an interpretation well explains the results of this study. Because there is no
401 resolution for the narrow central conduit of the rising plume in the tomographic inversions in the
402 current spatial scale, the feature of $V_{P\mathrm{h}} > V_{Pv}$ is expected to be dominant in RAN, reflecting the
403 properties in the surrounding wide areas. On the other hand, SWS measurements in Iceland
404 revealed N-S to NW-SE FPOs, which are interpreted to reflect the background mantle flow
405 (Figure 12e, Bjarnason et al., 2002). The SWS results are considered to reflect anisotropy at
406 depths shallower than 200 km (Bjarnason et al., 2002), but background mantle flow in the same
407 direction is also reported to exist at 600-km depth (Ito et al., 2014). The weak FVDs found in this
408 study are also in the same direction, supporting the existence of the background mantle flow
409 beneath Iceland.

410 Previous studies also suggested the presence of mantle plumes beneath the Jan Mayen
411 (e.g., Elkins et al., 2016; Schilling et al., 1999) and Svalbard hotspots (Toyokuni et al., 2020a).
412 In this study, a strong positive RAN ($V_{P\mathrm{h}} > V_{Pv}$) and a negligible AAN are found beneath these
413 hotspots, and so the existence of mantle plumes is more conclusive according to the same
414 interpretation as in the case of Iceland plume. In addition, unlike the case of Iceland plume, there

is no weak AAN reflecting the background mantle flow beneath the Jan Mayen hotspot. The AAN-SRT1 and AAN-SRT2 results show that if AAN is originally present beneath Jan Mayen, it can be sufficiently detected (Figures 12d and 12e). Therefore, this result may suggest that the Iceland plume and the Jan Mayen plume may belong to different plume systems. The difference between the Iceland and Jan Mayen plumes was also pointed out by geochemical studies due to their difference in magma composition (e.g., Schilling et al., 1999). Toyokuni et al. (2020b) also suggested that the Jan Mayen and Svalbard plumes are tributaries of the Greenland plume rising from the CMB beneath Greenland, and so the plume system is distinguishable from the rather isolated Iceland plume. The results of this study reinforce such previous interpretations.

In the cross-sections of the RAN and AAN tomography passing through Greenland and Iceland, or Greenland and Jan Mayen, CGLLVZ is clearly visible in the isotropic V_P image inside the lithosphere beneath Greenland, whose thickness is estimated to be >200 km V_P (Artemieva, 2019; Jakovlev et al., 2012). The origin of CGLLVZ is thought to be residual heat of the Iceland and Jan Mayen plumes (Toyokuni et al., 2020a). The RAN cross-sections show that the RAN strength, which is very strong beneath Iceland, suddenly weakens when entering CGLLVZ. This may be due to that CGLLVZ is currently out of the mantle plumes, reinforcing the interpretation of Toyokuni et al. (2020a).

6.3 Labrador Sea, Davis Strait, and Baffin Bay

Breakup between Greenland and Canada is estimated to have occurred during the Late Cretaceous to early Cenozoic (Henriksen et al., 2009), but the cause of the breakup is currently under debate. So far, two contradicting hypotheses have been proposed: active breakup caused by the rising Iceland plume beneath Davis Strait, and passive breakup caused by far-field plate forces. Peace et al. (2017) denied the mantle plume hypothesis by combining various

observations, and proposed that the breakup began in the Labrador Sea in the south by far-field plate forces, but it was blocked by a thick continental keel beneath Davis Strait and did not propagate to Baffin Bay in the north.

Our results show that the Labrador Sea is characterized by a strong positive RAN ($V_{P\mathrm{h}} > V_{Pv}$) and a negligible AAN, which is similar to the features of the mantle plume described in Section 6.2. In addition, the isotropic tomography shows a conduit-like low-V_P anomaly at depths ≤ 300 km (Figure S7), suggesting the existence of local mantle upwelling. On the other hand, beneath Baffin Bay, there is no characteristic aspect because the isotropic component is average, and both RAN and AAN are negligible. The AAN-SRT1 and AAN-SRT2 results show that if AAN is originally present beneath Baffin Bay and the Labrador Sea, it can be sufficiently detected (Figures 11d and 11e). Davis Strait, located between these two areas, exhibits a clear high-V_P corridor extending from land at depths of 160−430 km (Figure S7), suggesting the presence of cold and rigid rock bodies as mentioned by Peace et al. (2017). The AAN is remarkably strong only in this area, showing NE-SW to E-W FVDs that are continuous from the west coast of Greenland and Baffin Island, also supporting the existence of rock bodies. Such FVDs are considered to reflect fossil anisotropy of rock body and/or LPO by mantle flow. A positive RAN ($V_{P\mathrm{h}} > V_{Pv}$) continuing from the Labrador Sea is dominant in the south, but it becomes negligible in the north. Combining the above features, we suggest the following process of the breakup between Greenland and Canada: the opening of the Labrador Sea was initiated by a local mantle upwelling, but the rock body beneath Davis Strait prevented the northward propagation of the breakup, while the Baffin Bay opened by a passive rift due to far-field plate forces. This is in good agreement with the interpretation of Peace et al. (2017), but we suggest

the existence of a local mantle upwelling beneath the Labrador Sea, which could be the driving force of the breakup.

Traditionally, the Tertiary basalt province on the west coast of Greenland was thought to have been formed by the Iceland plume track. However, several recent studies do not support this interpretation (Martos et al., 2018; Toyokuni et al., 2020a). Locally enhanced magmatism due to the northward-propagating Labrador Sea rift is blocked beneath Davis Strait may be a rational explanation for the Tertiary basalt province and existence of hot springs on the west coast of Greenland. In addition, Toyokuni et al. (2020a) suggested that the high geothermal heat flux (Martos et al., 2018) and low-V_P in the Archean block in southern Greenland were caused by a selective heat transfer from a hot mantle material beneath the Labrador Sea. The existence of local mantle upwelling suggested by this study reinforces this possibility. Regarding the origin of this local mantle upwelling, further tomographic studies targeting much wider regions are required.

Figure 13 shows a comparison of our AAN tomographic images with simulation results of the mantle flow field due to the rising Iceland plume (Marquart et al., 2007). The FVDs beneath Greenland are in good agreement with the directions of mantle flow, except at a depth of 680 km, where our tomographic resolution is relatively lower. Because the strong AAN areas correspond to the NEG body and another rock body beneath Davis Strait, the resulting anisotropy may be strongly influenced by the fossil anisotropy and SPO in these bodies. However, the good agreement of our results with the mantle flow model suggests that the LPO due to the rising Iceland, Jan Mayen, and Svalbard plumes is detected by our anisotropic tomography.

7. Conclusions

The first 3-D *P*-wave RAN and AAN model beneath Greenland and its surrounding regions down to 750-km depth is obtained by inverting a large number of high-quality *P*-wave arrival-times of local earthquakes and relative travel-time residuals of teleseismic events recorded by the GLISN and other seismic stations. Our novel tomographic results reveal the following features.

(1) The NEG body distributed from Northeast Greenland to its offshore at depths ≤ ~500 km exhibits a strong negative RAN ($V_{P\mathrm{h}} < V_{Pv}$) and a strong AAN with N-S to NE-SW FVDs. Because the NEG body is considered as a remnant of oceanic lithosphere of the Iapetus Ocean closed at 490−390 Ma when Laurentia and Baltica collided, the RAN and AAN might reflect fossil anisotropy inside the oceanic lithosphere, SPO associated with the fold, and/or LPO associated with mantle flow due to the upper-mantle plume system such as the Iceland plume.

(2) Low-V_P zones beneath the Iceland, Jan Mayen, and Svalbard hotspots are characterized by a strong positive RAN ($V_{P\mathrm{h}} > V_{Pv}$) and negligible or weak AAN, which may reflect horizontal radial LPO and/or SPO centered at the rising mantle plumes. The existence of Svalbard plume was first suggested by Toyokuni et al. (2020a), but this study confirms it more concretely from the perspective of seismic anisotropy. Furthermore, a weak AAN is revealed only beneath Iceland, which is thought to reflect the background mantle flow. This locality might suggest differences of the Iceland plume system in the south and the Jan Mayen−Svalbard plume system in the north, as pointed out in Toyokuni et al. (2020b).

(3) The upper mantle beneath the Labrador Sea is characterized by isotropic low-V_P and a strong positive RAN ($V_{P\mathrm{h}} > V_{Pv}$) and a negligible AAN, suggesting the presence of local mantle upwelling. On the other hand, the upper mantle beneath Baffin Bay has an average isotropic

feature and no noticeable anisotropy. Davis Strait, located between these two regions, is characterized by isotropic high-V_P, a transitive RAN, and a strong AAN, suggesting the presence of cold rock bodies. These results suggest that breakup between Greenland and Canada might be caused as follows: the breakup started at the Labrador Sea because of local mantle upwelling, the northward propagation of the breakup was blocked at Davis Strait, and Baffin Bay was opened by far-field plate forces.

Acknowledgments

We are grateful to Drs. Dean Childs, Kevin Nikolaus, Kent Anderson, Masaki Kanao, Yoko Tono, Seiji Tsuboi, Robin Abbott, Kathy Young, Drew Abbott, Silver Williams, Jason Hebert, Tetsuto Himeno, Susan Whitley, Orlando Leone, Akram Mostafanejad, Kirsten Arnell, and other staff members at GLISN, IRIS/PASSCAL, CH2M HILL Polar Services, and Norlandair for their contributions to the field operations in Greenland. We thank the staff of the ISC, IRIS/DMC, and USGS for providing the open-access arrival-time and waveform data used in this study. Dr. Árni Hjartarson kindly provided the hot springs locations in Greenland. We appreciate Drs. Hiroshi Takenaka, Akira Hasegawa, Toru Matsuzawa, Ryota Takagi, Keisuke Yoshida, and Katsutada Kaminuma for helpful discussions. This work was partially supported by research grants from Japan Society for the Promotion of Science (Nos. 18K03794, 24403006, 23224012, and 26241010). The GMT (Wessel et al., 2013) and SAC (Goldstein et al., 2003) software packages are used in this study. Part of the arrival-time data are downloaded from the ISC (http://www.isc.ac.uk/). The waveform data are downloaded from the IRIS/DMC (https://ds.iris.edu/ds/nodes/dmc/). Part of the event data are also downloaded from the USGS (https://www.usgs.gov/). Archiving of data from this study is underway through Zenodo. Currently these data can be seen in Supporting Information for review purposes.

Author contributions

Conceptualization: Genti Toyokuni, Dapeng Zhao

Data curation: Genti Toyokuni

Formal analysis: Genti Toyokuni

Methodology: Genti Toyokuni, Dapeng Zhao

Resources: Genti Toyokuni, Dapeng Zhao

Visualization: Genti Toyokuni

Writing – original draft: Genti Toyokuni

Writing – review & editing: Genti Toyokuni, Dapeng Zhao

References

Artemieva, I. M. (2019). Lithosphere thermal thickness and geothermal heat flux in Greenland from a new thermal isostasy method. *Earth-Science Reviews*, 188, 469–481. https://doi.org/10.1016/j.earscirev.2018.10.015

Bjarnason, I. T., Silver, P. G., Rümpker, G., & Solomon, S. C. (2002). Shear wave splitting across the Iceland hot spot: Results from the ICEMELT experiment. Journal of Geophysical Research, 107(B12), 2382. https://doi.org/10.1029/2001JB000916

Clinton, J. F., Nettles, M., Walter, F., Anderson, K., Dahl-Jensen, T., Giardini, D., Govoni, A., Hanka, W., Lasocki, S., Lee, W. S., McCormack, D., Mykkeltveit, S., Stutzmann, E., & Tsuboi, S. (2014). Seismic network in Greenland monitors Earth and ice system. *Eos, Transactions, American Geophysical Union*, 95(2), 13–24. https://doi.org/10.1002/2014EO020001

549 Darbyshire, F. A., Dahl-Jensen, T., Larsen, T. B., Voss, P. H., & Joyal, G. (2018). Crust and
550 uppermost-mantle structure of Greenland and the Northwest Atlantic from Rayleigh wave
551 group velocity tomography. *Geophysical Journal International*, 212(3), 1546–1569.
552 https://doi.org/10.1093/gji/ggx479

553 Dumke, I., Burwicz, E. B., Berndt, C., Klaeschen, D., Feseker, T., Geissler, W. H., & Sarkar, S.
554 (2016). Gas hydrate distribution and hydrocarbon maturation north of the Knipovich
555 Ridge, western Svalbard margin. *Journal of Geophysical Research: Solid Earth*, 121(3),
556 1405–1424. https://doi.org/10.1002/2015JB012083

557 Elkins, L. J., Hamelin, C., Blichert-Toft, J., Scott, S. R., Sims, K. W. W., Yeo, I. A., Devey, C.
558 W., & Pedersen, R. B. (2016). North Atlantic hotspot-ridge interaction near Jan Mayen
559 Island. *Geochemical Perspectives Letters*, 2(1), 55–67.
560 http://dx.doi.org/10.7185/geochemlet.1606

561 Goldstein, P., Dodge, D., Firpo, M., & Minner, L. (2003). SAC2000: Signal processing and
562 analysis tools for seismologists and engineers. In W. H. K. Lee, H. Kanamori, P. C.
563 Jennings, & C. Kisslinger (Eds.), *International Geophysics* (Vol. 81, pp. 1613–1614).
564 London: Academic Press.

565 Gou, T., Zhao, D., Huang, Z., & Wang, L. (2019). Aseismic deep slab and mantle flow beneath
566 Alaska: Insight from anisotropic tomography. *Journal of Geophysical Research: Solid*
567 *Earth*, 124, 1700–1724. https://doi.org/10.1029/2018JB016639

568 Henriksen, N., Higgins, A. K., Kalsbeek, F., & Pulvertaft, T. C. R. (2009). *Greenland from*
569 *Archean to Quaternary, Descriptive Text to the 1995 Geological Map of Greenland,*

1:2 500 000, 126 pp. Copenhagen: Geological Survey of Denmark and Greenland. https://doi.org/10.1007/978-4-431-55360-1

Hjartarson, A., & Armannsson, H. (2010). *Geothermal research in Greenland*. Paper presented at World Geothermal Congress 2010, Bali, Indonesia.

Huang, Z., Zhao, D., & Wang, L. (2015). P wave tomography and anisotropy beneath Southeast Asia: Insight into mantle dynamics. *Journal of Geophysical Research: Solid Earth*, 120, 5154–5174. https://doi.org/10.1002/2015JB012098

Ishise, M., & Oda, H. (2005). Three-dimensional structure of P-wave anisotropy beneath Tohoku district, northeast Japan. *Journal of Geophysical Research*, 110, B07304. https://doi.org/10.1029/2004JB003599

Ito, G., Dunn, R., Li, A., Wolfe, C. J., Gallego, A., & Fu, Y. (2014). Seismic anisotropy and shear wave splitting associated with mantle plume-plate interaction. *Journal of Geophysical Research: Solid Earth*, 119, 4923–4937. https://doi.org/10.1002/2013JB010735

Jakovlev, A. V., Bushenkova, N. A., Koulakov, I. Yu., & Dobretsov, N. L. (2012). Structure of the upper mantle in the Circum-Arctic region from regional seismic tomography. *Russian Geology and Geophysics*, 53(10), 963–971. https://doi.org/10.1016/j.rgg.2012.08.001

Jiang, G., Zhao, D., & Zhang, G. (2009a). Seismic tomography of the Pacific slab edge under Kamchatka. *Tectonophysics*, 465(1–4), 190–203. https://doi.org/10.1016/j.tecto.2008.11.019

590 Jiang, G., Zhao, D., & Zhang, G. (2009b). Crustal correction in teleseismic tomography and its
591 application (in Chinese with English abstract). *Chinese Journal of Geophysics*, 52(6),
592 1508–1514. https://doi.org/10.3969/j.issn.0001-5733.2009.06.012

593 Jiang, G., Zhang, G., Zhao, D., Lü, Q., Li, H., & Li, X. (2015). Mantle dynamics and Cretaceous
594 magmatism in east-central China: Insight from teleseismic tomograms. *Tectonophysics*,
595 664, 256–268. https://doi.org/10.1016/j.tecto.2015.09.019

596 Karato, S., Jung, H., Katayama, I., & Skemer, P. (2008). Geodynamic significance of seismic
597 anisotropy of the upper mantle: New insights from laboratory studies. *Annual Review of*
598 *Earth and Planetary Sciences*, 36(1), 59–95.
599 https://doi.org/10.1146/annurev.earth.36.031207.124120

600 Katayama, I., & Karato, S. (2006). Effect of temperature on the B- to C-type olivine fabric
601 transition and implication for flow pattern in subduction zones. *Physics of the Earth and*
602 *Planetary Interiors*, 157(1–2), 33–45. https://doi.org/10.1016/j.pepi.2006.03.005

603 Kumar, P., Kind, R., Priestley, K., & Dahl-Jensen, T. (2007). Crustal structure of Iceland and
604 Greenland from receiver function studies. *Journal of Geophysical Research: Solid Earth*,
605 112(B3), B03301. https://doi.org/10.1029/2005JB003991

606 Lebedev, S., Schaeffer, A. J., Fullea, J., & Pease, V. (2017). Seismic tomography of the Arctic
607 region: inferences for the thermal structure and evolution of the lithosphere. *Geological*
608 *Society, London, Special Publications*, 460, 419–440. https://doi.org/10.1144/SP460.10

609 Levshin, A. L., Shen, W., Barmin, M. P., & Ritzwoller, M. H. (2017). Surface wave studies of
610 the Greenland upper lithosphere using ambient seismic noise.
611 https://pdfs.semanticscholar.org/977c/ce2101b7f9b384d38e9b051bf289a7277b54.pdf

612 Liu, X., & Zhao, D. (2017). P-wave anisotropy, mantle wedge flow and olivine fabrics beneath
613 Japan. *Geophysical Journal International*, 210, 1410-1431.
614 https://doi.org/10.1093/gji/ggx247

615 Long, M. D., & Becker, T. W. (2010). Mantle dynamics and seismic anisotropy. *Earth and*
616 *Planetary Science Letters*, 297(3–4), 341–354. https://doi.org/10.1016/j.epsl.2010.06.036

617 Marquart, G., Schmeling, H., & Čadek, O. (2007). Dynamic models for mantle flow and seismic
618 anisotropy in the North Atlantic region and comparison with observations. *Geochemistry,*
619 *Geophysics, Geosystems*, 8, Q02008. https://doi.org/10.1029/2006GC001359

620 Martos, Y. M., Jordan, T. A., Catalán, M., Jordan, T. M., Bamber, J. L., & Vaughan, D. G.
621 (2018). Geothermal heat flux reveals the Iceland hotspot track underneath Greenland.
622 *Geophysical Research Letters*, 45, 8214–8222. https://doi.org/10.1029/2018GL078289

623 Metelkin, D. V., Vernikovsky, V. A., & Matushkin, N. Yu. (2015). Arctida between Rodinia and
624 Pangea. *Precambrian Research*, 259, 114–129.
625 https://doi.org/10.1016/j.precamres.2014.09.013

626 Mordret, A. (2018). Uncovering the Iceland hot spot track beneath Greenland. *Journal of*
627 *Geophysical Research: Solid Earth*, 123, 4922–4941.
628 https://doi.org/10.1029/2017JB015104

629 Mordret, A., Mikesell, T. D., Harig, C., Lipovsky, B. P., & Prieto, G. A. (2016). Monitoring
630 southwest Greenland's ice sheet melt with ambient seismic noise. *Science Advances*,
631 2(5), e1501538. http://dx.doi.org/10.1126/sciadv.1501538

Okaya, D., Vel, S. S., Song, W. J., & Johnson, S. E. (2018). Modification of crustal seismic anisotropy by geological structures ("structural geometric anisotropy"). *Geosphere*, 15(1), 146–170. https://doi.org/10.1130/GES01655.1

Paige, C. C., & Saunders, M. A. (1982). LSQR, An algorithm for sparse linear equations and sparse least squares. *ACM Transactions on Mathematical Software (TOMS)*, 8(1), 43–71. https://doi.org/10.1145/355984.355989

Peace, A. L., Foulger, G. R., Schiffer, C., & McCaffrey, K. J. (2017). Evolution of Labrador Sea–Baffin Bay: Plate or plume processes? *Geoscience Canada*, 44(3), 91–102. https://doi.org/10.12789/geocanj.2017.44.120

Portnov, A., Vadakkepuliyambatta, S., Mienert, J., & Hubbard, A. (2016). Ice-sheet-driven methane storage and release in the Arctic. *Nature Communications*, 7, 10314. https://doi.org/10.1038/ncomms10314

Pourpoint, M., Anandakrishnan, S., Ammon, C. J., & Alley, R. B. (2018). Lithospheric structure of Greenland from ambient noise and earthquake surface wave tomography. *Journal of Geophysical Research: Solid Earth*, 123, 7850–7876. https://doi.org/10.1029/2018JB015490

Rickers, F., Fichtner, A., & Trampert, J. (2013). The Iceland–Jan Mayen plume system and its impact on mantle dynamics in the North Atlantic region: Evidence from full-waveform inversion. *Earth and Planetary Science Letters*, 367, 39–51. https://doi.org/10.1016/j.epsl.2013.02.022

Schilling, J.-G., Kingsley, R., Fontignie, D., Poreda, R., & Xue, S. (1999). Dispersion of the Jan Mayen and Iceland mantle plumes in the Arctic: A He-Pb-Nd-Sr isotope tracer study of

basalts from the Kolbeinsey, Mohns, and Knipovich Ridges. *Journal of Geophysical Research*, 104(B5), 10543–10569. https://doi.org/10.1029/1999JB900057

Takenaka, H., Komatsu, M., Toyokuni, G., Nakamura, T., & Okamoto, T. (2017). Quasi-Cartesian finite-difference computation of seismic wave propagation for a three-dimensional sub-global model. *Earth, Planets and Space*, 69, 67. https://doi.org/10.1186/s40623-017-0651-1

Thiede, J., Eldholm, O., & Myhre, A. M. (2011). Chapter 46 Scientific deep-sea drilling in high northern latitudes. *Geological Society, London, Memoirs*, 35, 703–714. https://doi.org/10.1144/M35.46

Toyokuni, G., Kanao, M., Tono, Y., Himeno, T., Tsuboi, S., Childs, D., Anderson, K., & Takenaka, H. (2014). Monitoring of the Greenland ice sheet using a broadband seismometer network: the GLISN project. *Antarctic Record*, 58(1), 1–18. http://doi.org/10.15094/00009722

Toyokuni, G., Komatsu, M., & Takenaka, H. (2021). Estimation of seismic attenuation of the Greenland Ice Sheet using 3-D waveform modeling. *Journal of Geophysical Research: Solid Earth*. https://doi.org/10.1029/2021JB021694

Toyokuni, G., Matsuno, T., & Zhao, D. (2020a). *P* wave tomography beneath Greenland and surrounding regions: 1. Crust and upper mantle. *Journal of Geophysical Research: Solid Earth*, 125, e2020JB019837. https://doi.org/10.1029/2020JB019837

Toyokuni, G., Matsuno, T., & Zhao, D. (2020b). *P* wave tomography beneath Greenland and surrounding regions: 2. Lower mantle. *Journal of Geophysical Research: Solid Earth*, 125, e2020JB019839. https://doi.org/10.1029/2020JB0198379

676 Toyokuni, G., Takenaka, H., Kanao, M., Tsuboi, S., & Tono, Y. (2015). Numerical modeling of
677 seismic waves for estimating the influence of the Greenland ice sheet on observed
678 seismograms. *Polar Science*, 9(1), 80–93. https://doi.org/10.1016/j.polar.2014.12.001

679 Toyokuni, G., Takenaka, H., Takagi, R., Kanao, M., Tsuboi, S., Tono, Y., Childs, D., & Zhao, D.
680 (2018). Changes in Greenland ice bed conditions inferred from seismology. *Physics of*
681 *the Earth and Planetary Interiors*, 277, 81–98. https://doi.org/10.1016/j.pepi.2017.10.010

682 Ucisik, N., Gudmundsson, Ó., Priestley, K., & Larsen, T. B. (2005). Seismic anisotropy beneath
683 east Greenland revealed by shear wave splitting. *Geophysical Research Letters*, 32,
684 L08315. https://doi.org/10.1029/2004GL021875

685 Ucisik, N., Gudmundsson, Ó., Hanka, W., Dahl-Jensen, T., Mosegaard, K., & Priestley, K.
686 (2008). Variations of shear-wave splitting in Greenland: Mantle anisotropy and possible
687 impact of the Iceland plume. *Tectonophysics*, 462(1–4), 137–148.
688 https://doi.org/10.1016/j.tecto.2007.11.074

689 Um, J., & Thurber, C. (1987). A fast algorithm for two-point seismic ray tracing. *Bulletin of the*
690 *Seismological Society of America*, 77(3), 972–986.

691 Wang, J., & Zhao, D. (2008). P-wave anisotropic tomography beneath Northeast Japan. *Physics*
692 *of the Earth and Planetary Interiors*, 170(1–2), 115–133.
693 https://doi.org/10.1016/j.pepi.2008.07.042

694 Wang, J., & Zhao, D. (2013). P-wave tomography for 3-D radial and azimuthal anisotropy of
695 Tohoku and Kyushu subduction zones. *Geophysical Journal International*, 193(3), 1166–
696 1181. https://doi.org/10.1093/gji/ggt086

697 Wang, Z. W., & Zhao, D. (2021). 3D anisotropic structure of the Japan subduction zone. *Science*
698 *Advances*, 7, eabc9620. https://doi.org/10.1126/sciadv.abc9620

Wessel, P., Smith, W. H. F., Scharroo, R., Luis, J., & Wobbe, F. (2013). Generic Mapping Tools: Improved Version Released. *Eos, Transactions, American Geophysical Union*, 94(45), 409. https://doi.org/10.1002/2013EO450001

Zhang, H., Zhao, D., Ju, C., Li, Y. E. Li, G., Ding, M., Chen, S., & Zhao, J. (2020). Upper mantle deformation of the Terror Rift and northern Transantarctic Mountains in Antarctica: Insight from *P* wave anisotropic tomography. *Geophysical Research Letters*, 47, e2019GL086511. https://doi.org/10.1029/2019GL086511

Zhao, D. (2015). *Multiscale Seismic Tomography*, 304 pp. Tokyo: Springer. https://doi.org/10.1007/978-4-431-55360-1

Zhao, D., Hasegawa, A., & Horiuchi, S. (1992). Tomographic imaging of P and S wave velocity structure beneath northeastern Japan. *Journal of Geophysical Research*, 97(B13), 19909–19928. https://doi.org/10.1029/92JB00603

Zhao, D., Hasegawa, A., & Kanamori, H. (1994). Deep structure of Japan subduction zone as derived from local, regional, and teleseismic events. *Journal of Geophysical Research: Solid Earth*, 99(B11), 22313–22329. https://doi.org/10.1029/94JB01149

Zhao, D., Yanada, T., Hasegawa, A., Umino, N., & Wei, W. (2012). Imaging the subducting slabs and mantle upwelling under the Japan Islands. *Geophysical Journal International*, 190(2), 816–828. https://doi.org/10.1111/j.1365-246X.2012.05550.x

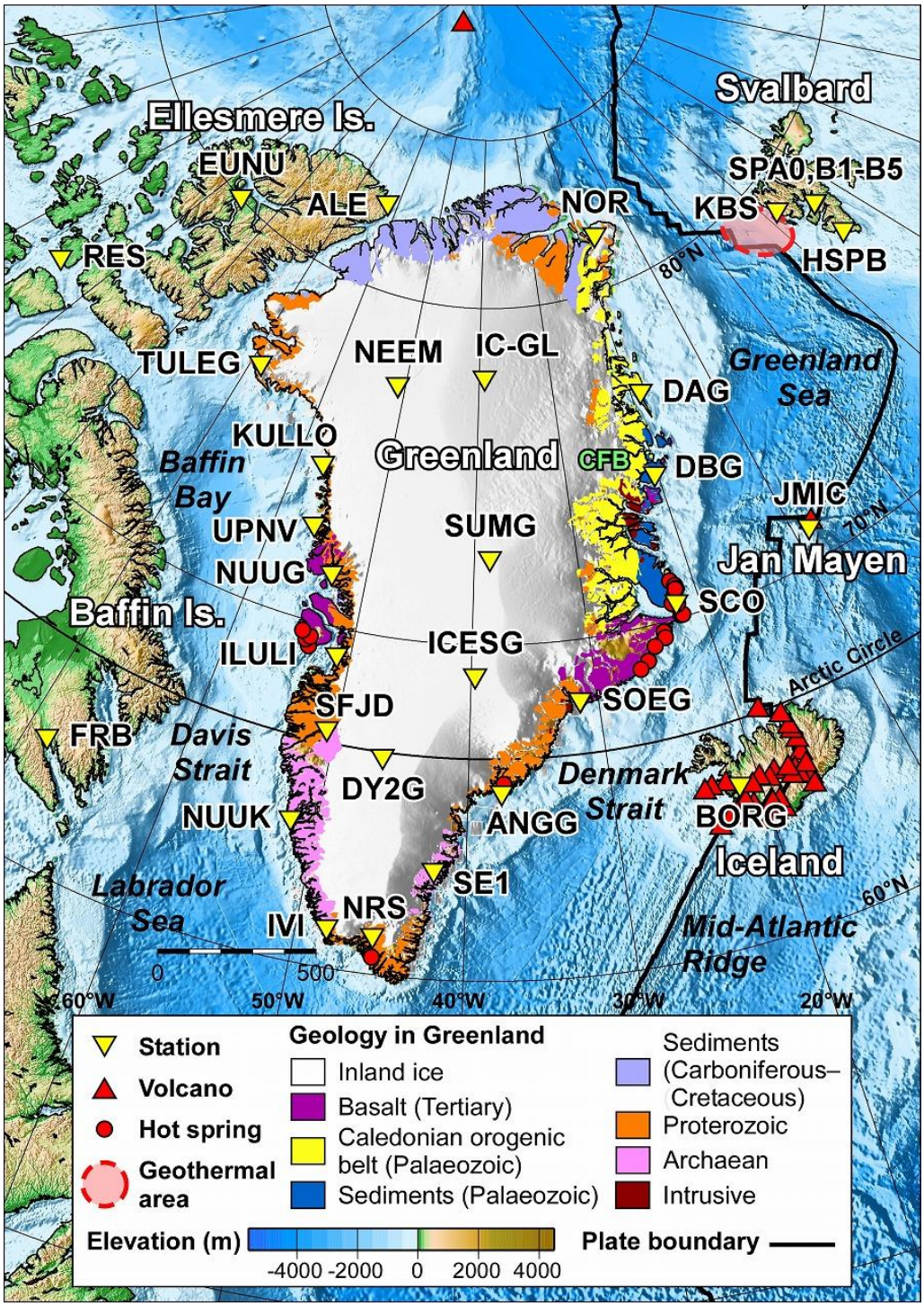

721

722 **Figure 1**. Map of Greenland and its surrounding regions. White color denotes the Greenland ice

723 sheet (GrIS). Yellow triangles: seismic stations used in this study; red triangles: active

724 volcanoes; red dots: hot springs. The red dashed line shows the Svalbard geothermal area
725 (Dumke et al., 2016; Portnov et al., 2016). Geological map of Greenland (Kumar et al., 2007) is
726 also shown. CFB = Caledonian fold belt.
727
728
729
730
731
732
733
734
735
736
737
738
739
740
741
742
743

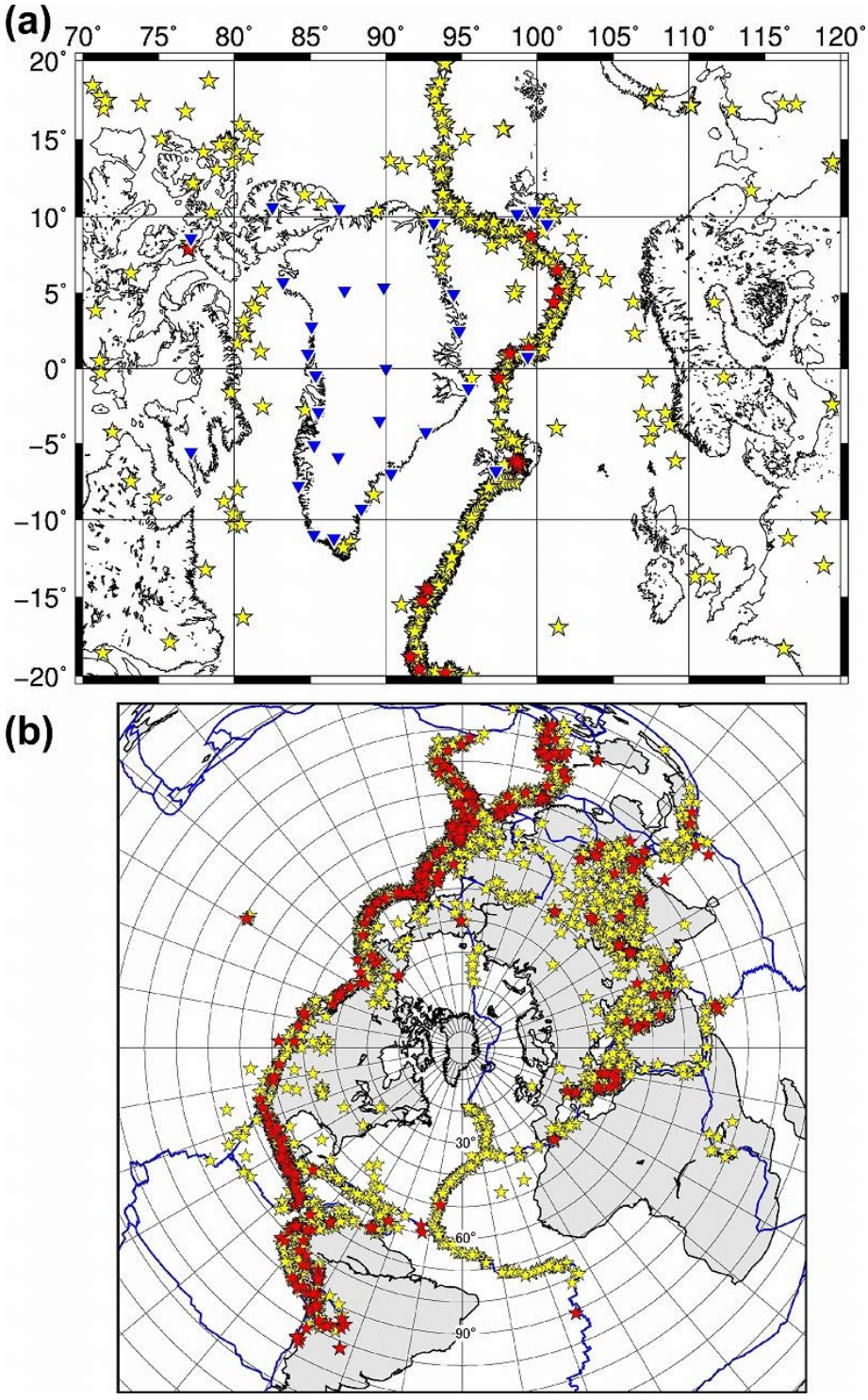

744

745 **Figure 2**. Epicentral distribution of **(a)** local earthquakes and **(b)** teleseismic events used in this

746 study. The panel (a) also displays longitudinal and latitudinal ranges of our study region. In (a),

yellow stars: 1,288 events from the ISC-EHB catalog; red stars: 21 events whose arrival times were manually picked by the authors. In (b), red circles: 6,884 events from the ISC-EHB catalog; red stars: 347 events whose arrival times were picked by Toyokuni et al. (2020a) using a waveform cross-correlation method.

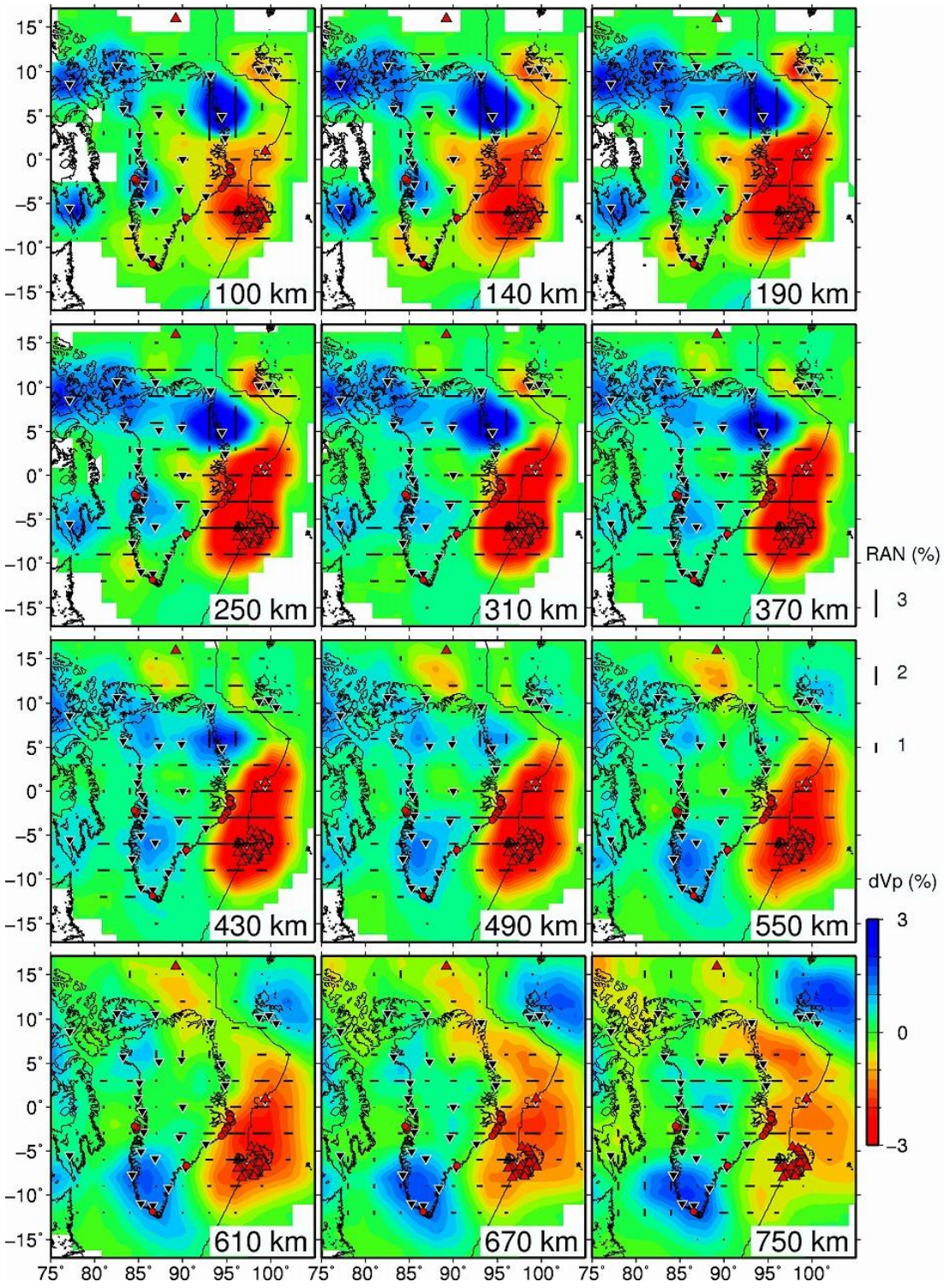

767

768 **Figure 3**. Map view images of V_P radial anisotropy (RAN) tomography. The layer depth is

769 shown at the lower-right corner of each panel. Blue and red colors denote high and low isotropic

770 V_P perturbations, respectively, whose scale (in %) is shown on the right. The length of black bars
771 denotes the RAN amplitude, whose scale (in %) is also shown on the right. The horizontal and
772 vertical bars denote positive RAN ($V_{P\mathrm{h}} > V_{Pv}$) and negative RAN ($V_{P\mathrm{h}} < V_{Pv}$), respectively.
773 Areas with hit counts < 5 are masked in white. The red triangles, red dots, black triangles, and
774 thin black lines denote active volcanoes, hot springs, seismic stations, and plate boundaries,
775 respectively.
776
777
778
779
780
781
782
783
784
785
786
787
788
789

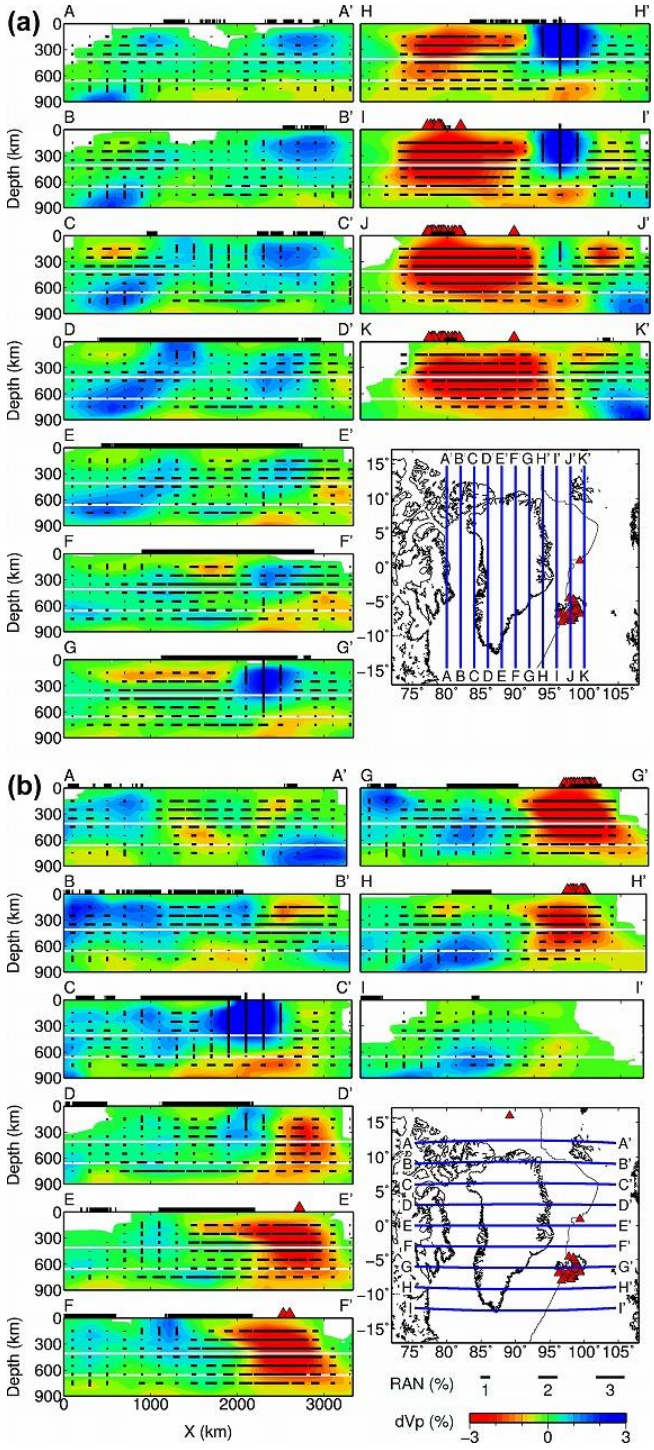

Figure 4. Vertical cross-sections of V_P radial anisotropy (RAN) tomography along **(a)** eleven N-S oriented profiles and **(b)** nine E-W oriented profiles. Locations of the profiles are shown on the

inset maps. Blue and red colors denote high and low isotropic V_P perturbations, respectively, whose scale (in %) is shown at the bottom. The length of black bars denotes the RAN amplitude, whose scale (in %) is also shown at the bottom. The horizontal and vertical bars denote positive RAN ($V_{P\mathrm{h}} > V_{Pv}$) and negative RAN ($V_{P\mathrm{h}} < V_{Pv}$), respectively. Areas with hit counts < 5 are masked in white. The 410-km and 660-km discontinuities are indicated by white solid lines. The thick black lines on the surface denote land areas. Active volcanoes within a ±2° width of each profile are shown as red triangles.

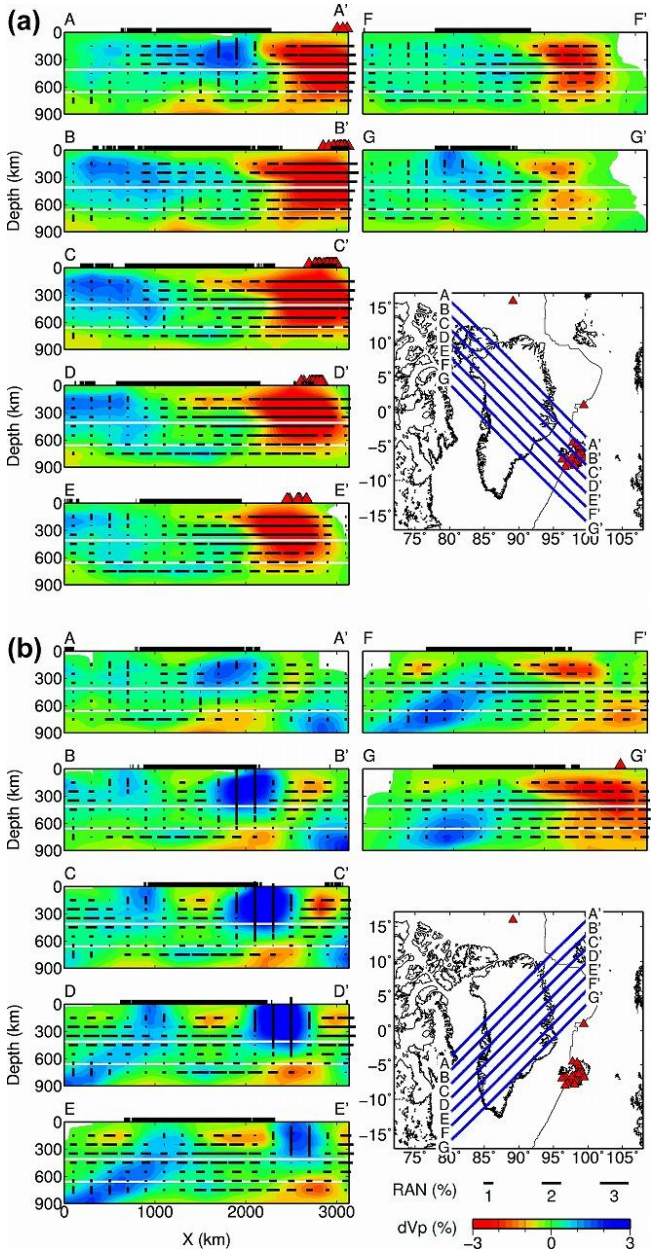

Figure 5. Same as Figure 4 but along **(a)** seven NW-SE oriented profiles and **(b)** seven NE-SW oriented profiles.

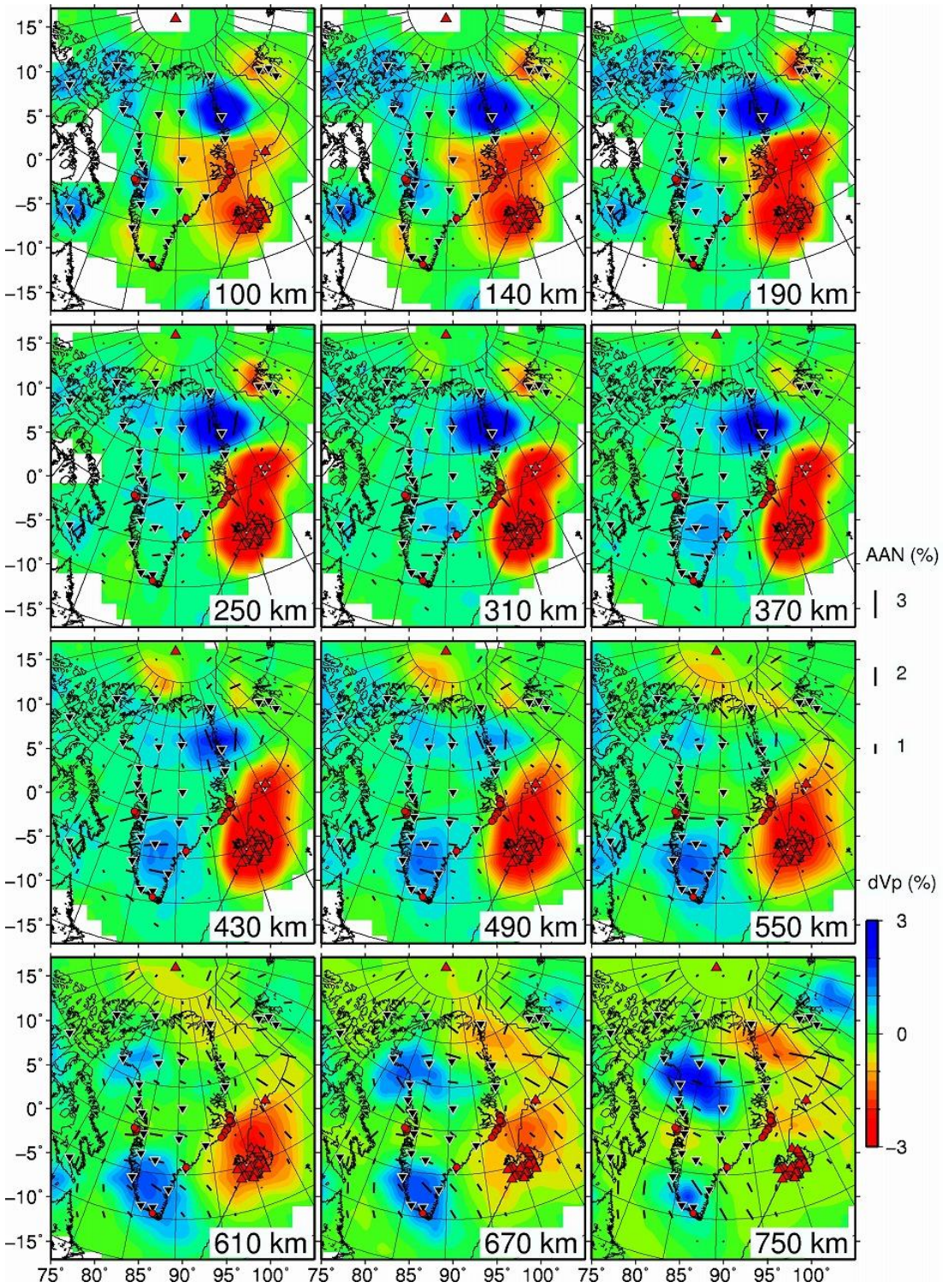

Figure 6. Same as Figure 3 but for V_P azimuthal anisotropy (AAN) tomography. The length of black bars denotes the AAN amplitude, whose scale (in %) is shown on the right. The bar

orientation denotes fast-velocity direction (FVD). The other symbols are the same as those in Figure 3 except for displaying the meridian of the geographical coordinates so that the FVDs are more visible.

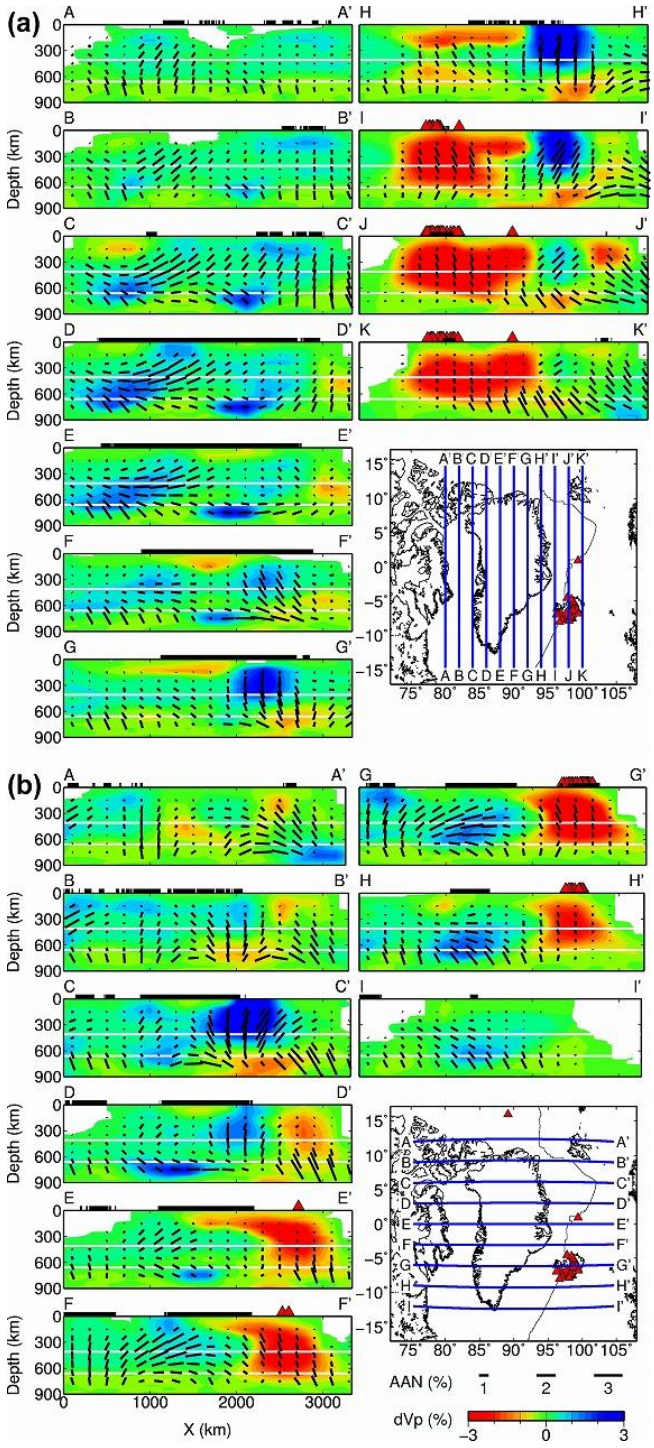

841

842 **Figure 7**. Same as Figure 4 but for V_P azimuthal anisotropy (AAN) tomography. The length of

843 black bars denotes the AAN amplitude, whose scale (in %) is shown on the right. The bar

orientation denotes fast-velocity direction (FVD): vertical bars denote N-S FVDs, whereas horizontal bars denote E-W FVDs. The other symbols are the same as those in Figure 5.

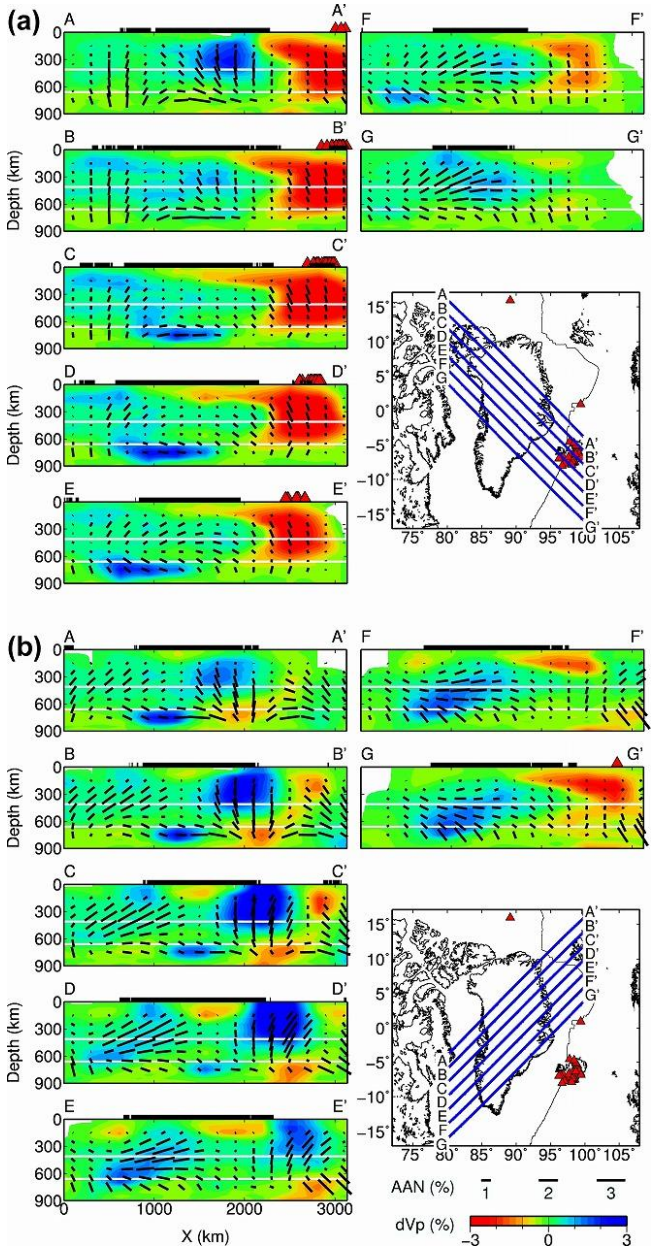

Figure 8. Same as Figure 7 but along **(a)** seven NW-SE oriented profiles and **(b)** seven NE-SW oriented profiles.

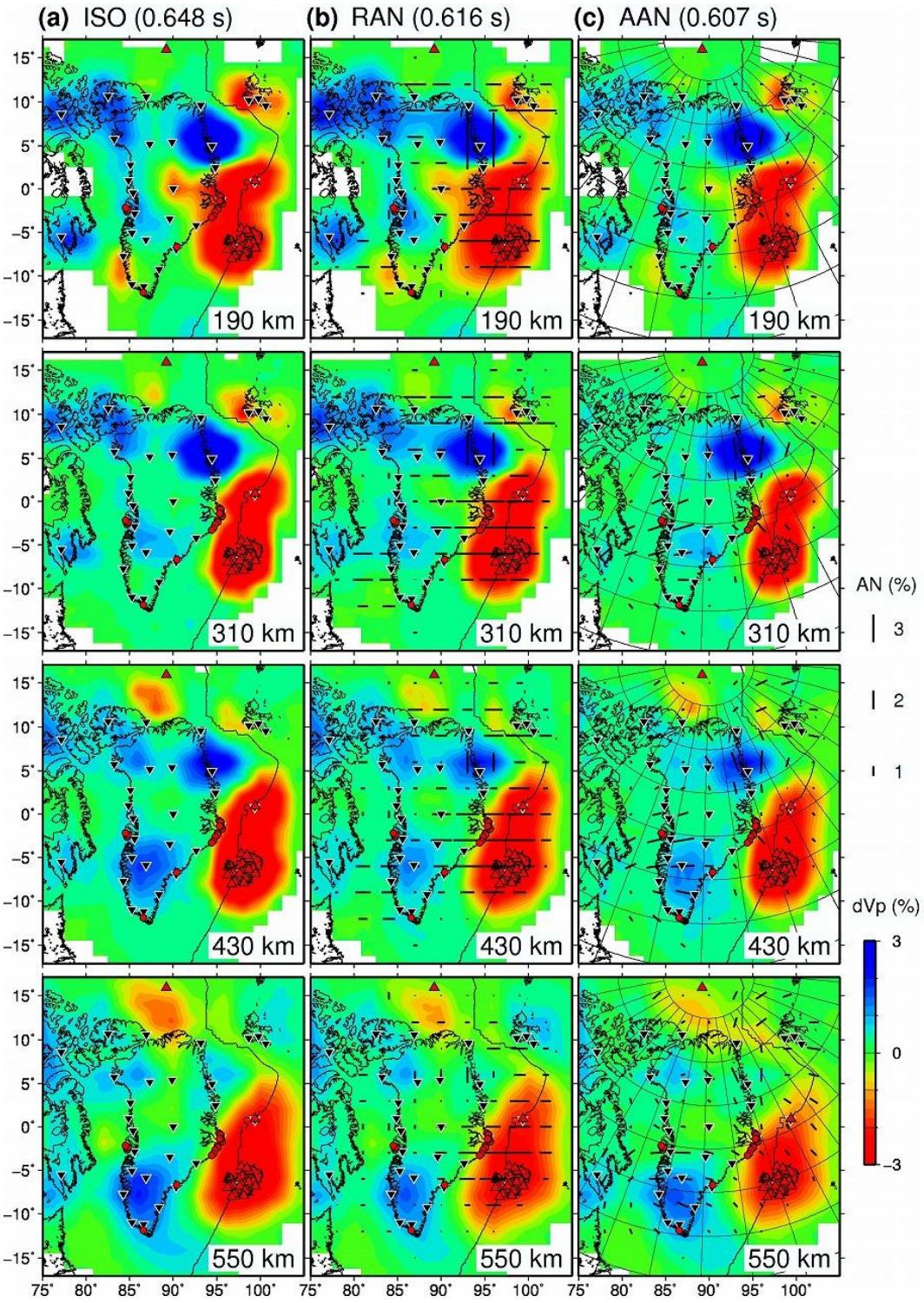

869

870 **Figure 9**. Comparison of **(a)** isotropic V_P tomography, **(b)** V_P radial anisotropy (RAN)

871 tomography, and **(c)** V_P azimuthal anisotropy (AAN) tomography with the same 3-D grids, and

the same damping and smoothing parameters. The layer depth is shown at the lower-right corner of each panel.

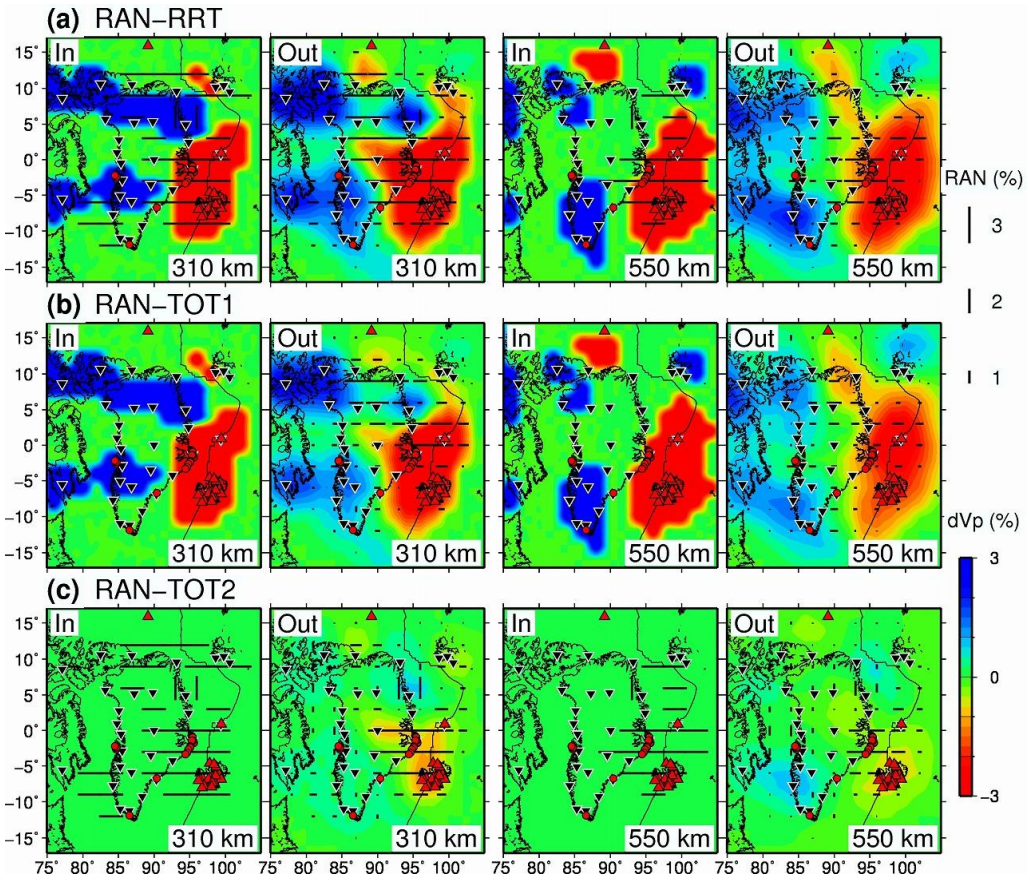

Figure 10. Summary of the resolution tests for V_P radial anisotropy (RAN) tomography. Map view images of the input (left panels) and output (right panels) models of the **(a)** RAN-RRT, **(b)** RAN-TOT1, and **(c)** RAN-TOT2 at depths of 310 km and 550 km. The layer depth is shown at the lower-right corner of each panel. The scales and symbols are the same as those in Figure 3.

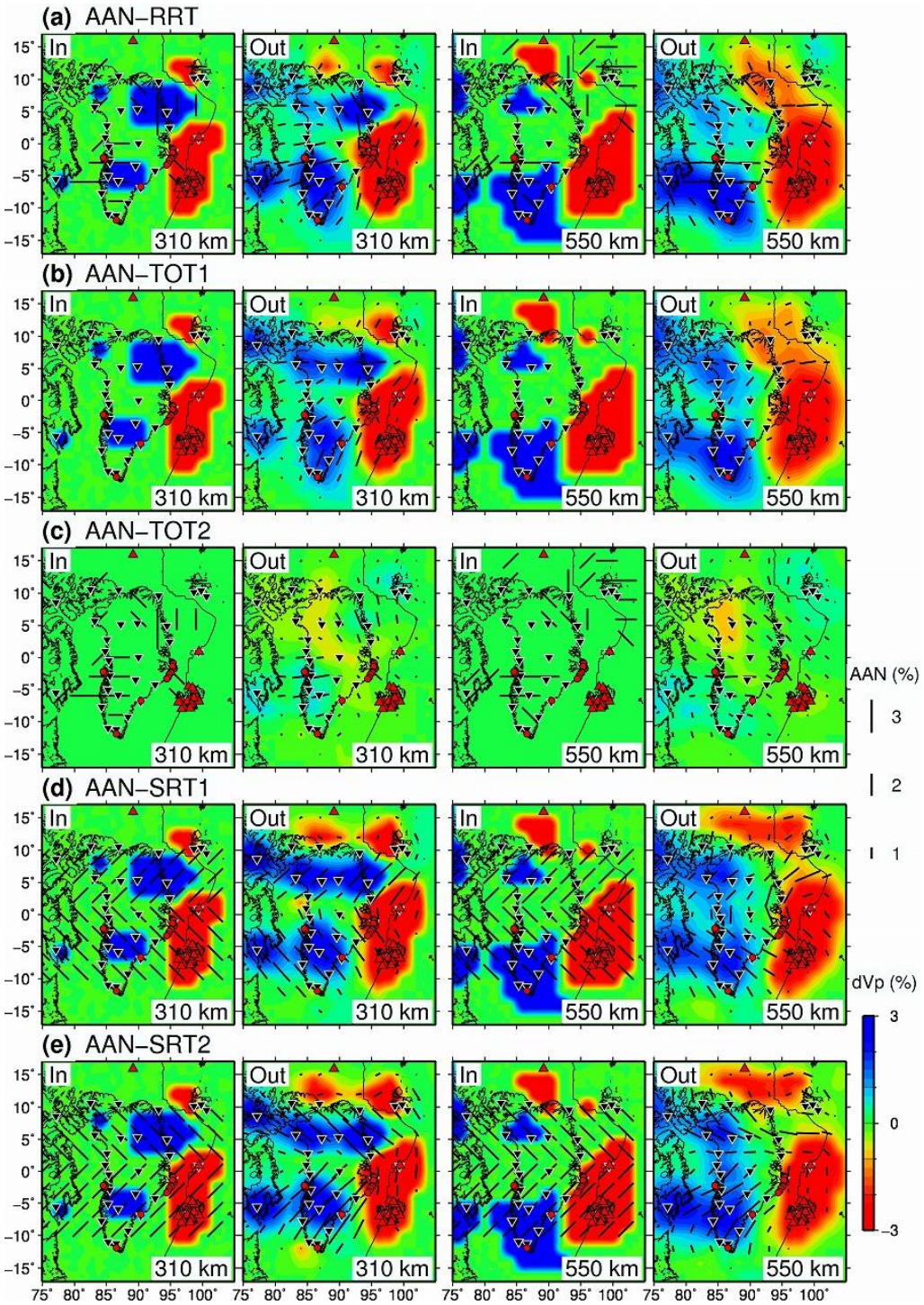

902

903 **Figure 11**. Summary of the resolution tests for V_P azimuthal anisotropy (AAN) tomography.

904 Map view images of the input (left panels) and output (right panels) models of the **(a)** AAN-RRT,

905 **(b)** AAN-TOT1, **(c)** AAN-TOT2, **(d)** AAN-SRT1, and **(e)** AAN-SRT2 at depths of 310 km and
906 550 km. The layer depth is shown at the lower-right corner of each panel. The scales and
907 symbols are the same as those in Figure 6.
908
909
910
911
912
913
914
915
916
917
918
919
920
921
922
923
924

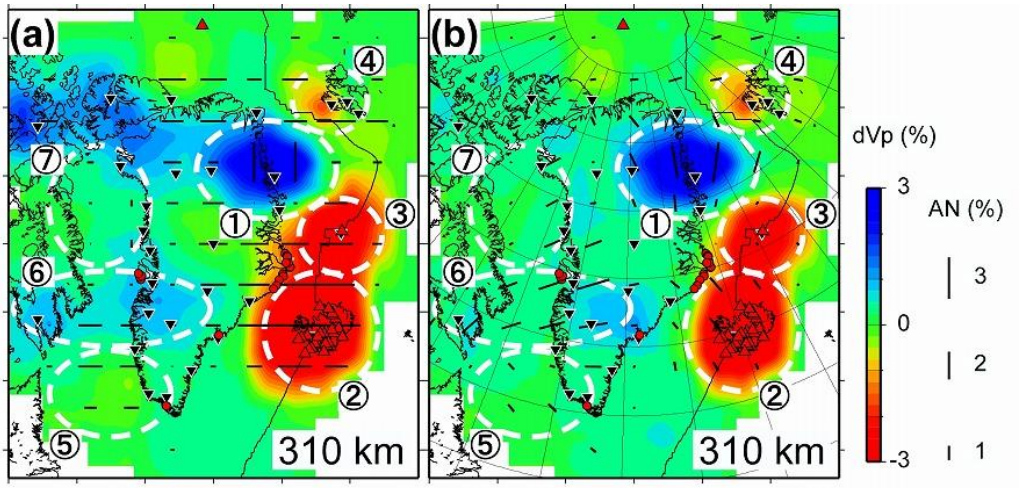

(c)

Num	Region	Isotropic	RAN	AAN
①	NEG body	High-V	Strong −	Strong N-S to NE-SW
②	Iceland hotspot	Low-V	Strong +	Weak N-S to NW-SE
③	Jan Mayen hotspot	Low-V	Strong +	Negligible
④	Svalbard hotspot	Low-V	Strong +	Negligible
⑤	Labrador Sea	Low-V	Strong +	Negligible
⑥	Davis Strait	High-V	Strong + (South) Negligible (North)	Strong NE-SW to E-W
⑦	Baffin Bay	Average	Negligible	Negligible

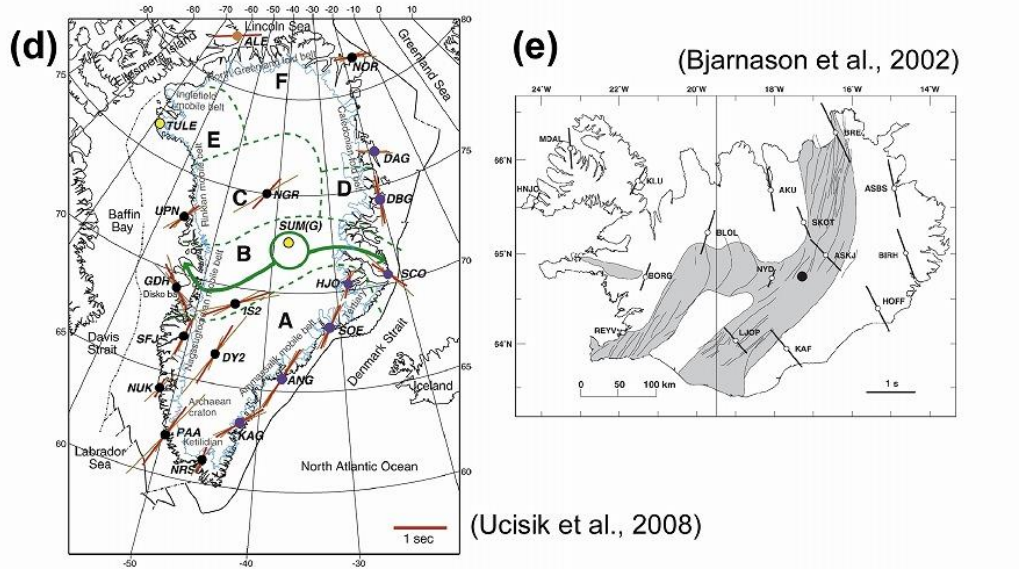

925

926 **Figure 12**. Main features of seismic anisotropy obtained by this study and comparison with shear

927 wave splitting (SWS) measurements. Map view images of **(a)** V_P radial anisotropy (RAN)

928 tomography and **(b)** V_P azimuthal anisotropy (AAN) tomography at 310-km depth obtained by
929 this study. The scales are shown on the right. The major regions are numbered 1−7, whose
930 features are summarized in **(c)**. The other symbols are the same as those in Figures 3 and 6. **(d)**
931 SWS measurements at 20 stations in Greenland (Ucisik et al., 2008). The thick red bars denote
932 the fast-polarization orientation whose length showing the time delay, whereas the thin brown
933 bars denote their 2σ uncertainties. The yellow dots denote stations where the SWS is not
934 observed. **(e)** SWS measurements at 16 stations in Iceland (Bjarnason et al., 2002). The thick
935 black bars denote the fast-polarization orientation whose length showing the time delay.
936
937
938
939
940
941
942
943
944
945
946
947

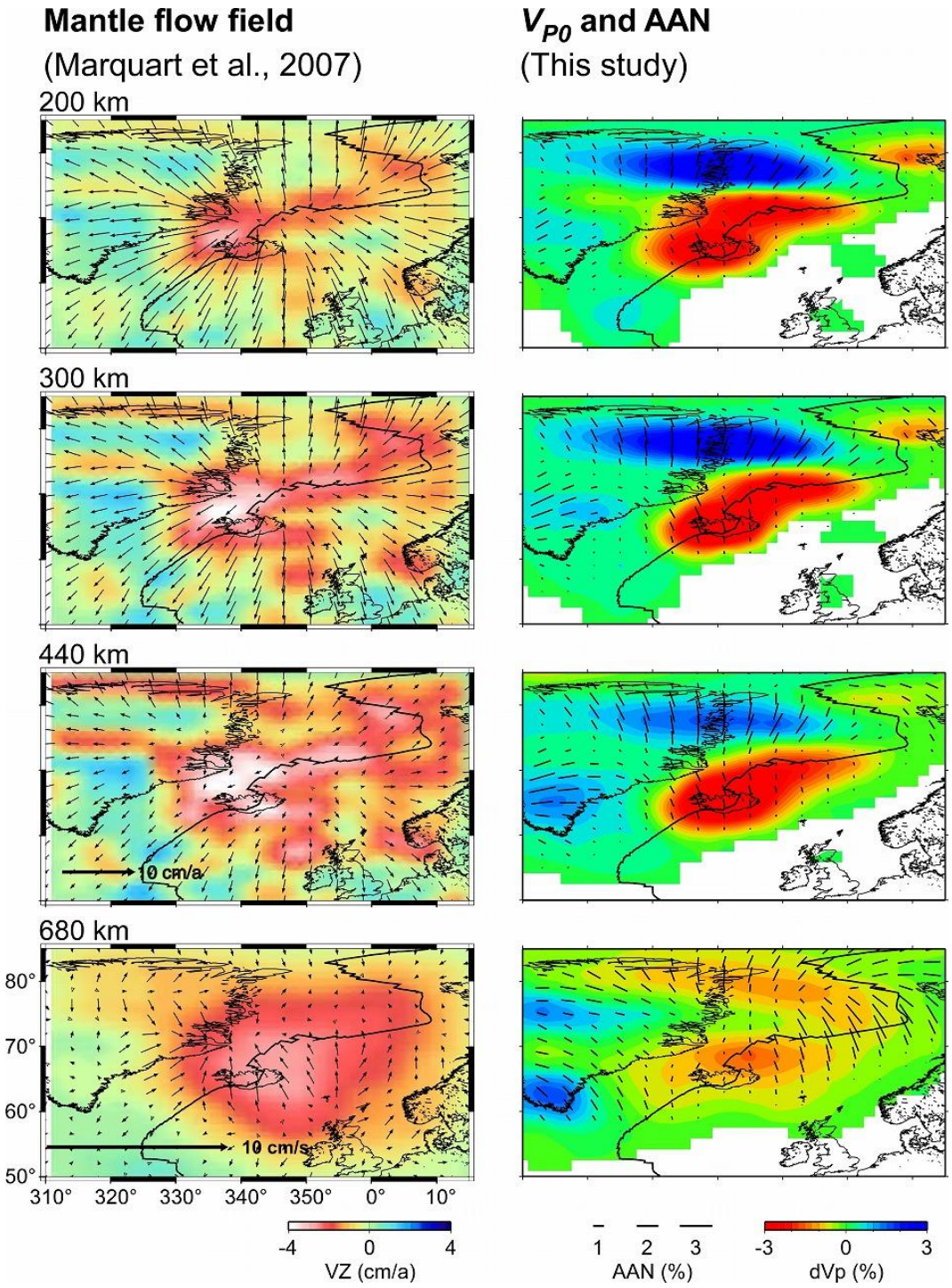

948

949 **Figure 13**. Comparison of the mantle flow field simulated by Marquart et al. (2007) (left) with

950 V_P azimuthal anisotropy (AAN) tomography obtained by this study (right). The layer depth is

951 shown above each map on the left. In the mantle flow field, horizontal flow is shown by arrows
952 whose scales are displayed on the 440-km map for the upper mantle, and on the 680-km map for
953 the lower mantle; vertical flow is shown by colors whose scale is shown at the bottom-left. The
954 AAN tomographic images are the same as those in Figure 6 except that they are displayed in the
955 Cartesian coordinates.
956
957
958
959
960
961
962
963
964
965
966
967
968
969
970

971

972

973 **Table 1**. Information on the eight resolution tests conducted by this study.

Name	Description of the initial model
RAN-RRT	Restoring resolution test. Highlights the pattern of actual RAN tomographic results. Isotropic component: Contains high-V_{P0} (+3%) and low-V_{P0} (−3%). Anisotropic component: Contains positive α (+2%) and negative α (−2%).
RAN-TOT1	Trade-off test. Similar to the RAN_RRT model, but without the anisotropic component.
RAN-TOT2	Trade-off test. Similar to the RAN_RRT model, but without the isotropic component.
AAN-RRT	Restoring resolution test. Highlights the pattern of actual AAN tomographic results. Isotropic component: Contains high-V_{P0} (+3%) and low-V_{P0} (−3%). Anisotropic components: β = +2%, ψ = −45°, 0°, 45°, or 90°.
AAN-TOT1	Trade-off test. Similar to the AAN_RRT model, but without the anisotropic components.
AAN-TOT2	Trade-off test. Similar to the AAN_RRT model, but without the isotropic component.
AAN-SRT1	Synthetic resolution test. The model contains the following structures: Isotropic component: Same as the AAN_RRT Anisotropic components: β = +2%, ψ = 45° for a region in the longitude range 90°−100° and latitude range 0°−10°, and ψ = −45° for a region in the longitude range 80°−90° and latitude range −10°−0°.
AAN-SRT2	Synthetic resolution test. The model contains the following structures: Isotropic component: Same as the AAN_RRT Anisotropic components: β = +2%, ψ = −45° for a region in the longitude range 90°−100° and latitude range 0°−10°, and ψ = 45° for a region in the longitude range 80°−90° and latitude range −10°−0°.

974